Chapter 4:

Validation of pharmacophore-identified inhibitors against *Plasmodium falciparum* SpdS with X-ray crystallography

4.1. Introduction

The ensemble of the polyamines; putrescine, spermidine and spermine has been shown to occur in millimolar concentrations within the parasite and correspondingly increase during the asexual, intra-erythrocytic developmental cycle of the parasite [10,67,100]. Upstream precursor metabolites required for the synthesis of polyamines including L-ornithine as substrate also increase during maturation of the parasites [214]. The stoichiometric by-product of spermidine formation, MTA, is catabolised and recycled to adenine and methionine within the parasites [215]. The level of spermidine exceeds that of other polyamines, emphasising the role of *Pf*SpdS as a major polyamine flux determining protein [100]. Additionally, spermidine appears to have greater metabolic importance compared to the other polyamines as it is a prerequisite for the post-translational activation of eIF-5A (involved in translation initiation and elongation [216]) and in trypanosomes for the biosynthesis of the gluthathione mimic, trypanothione [217]. Some effects of polyamine biosynthesis inhibitors have therefore been attributed to the accumulation of unmodified eIF-5A due to spermidine depletion while null mutants of SpdS have also demonstrated their essential role in the survival of *L. donovani* parasites [218]. Moreover, in the plasmodial parasite, biosynthesis of spermine has also been attributed to the action of *Pf*SpdS [98], highlighting that attenuation of this protein holds promise to disrupt not only spermidine-dependent processes but also the formation of the downstream spermine metabolite [219].

The design of SpdS inhibitors has proven more challenging than expected with the most effective compound being 4MCHA (K_i of 1.4 µM, Figure 4.1)[220]. Throughout the 1980s and early 1990s various putrescine and dcAdoMet analogues were synthesised but none were found to inhibit SpdS activity within the nanomolar range [221-226]. However, with the release of the first SpdS crystal structure from *T. maritima* (1JQ3) in 2002, which was co-crystallised with the multi-substrate, transition state analogue AdoDATO (Figure 4.1) [132], SpdS has again received attention. This is moreover evidenced by the release of 38 SpdS crystal structures of which ten are from *H. sapiens* and seven are from *P. falciparum*. Furthermore, *Pf*SpdS and its importance as a possible drug target has also been revisited in the last couple of years with the use of transcriptomics and inhibitor co-crystallisation studies [119,182,227].

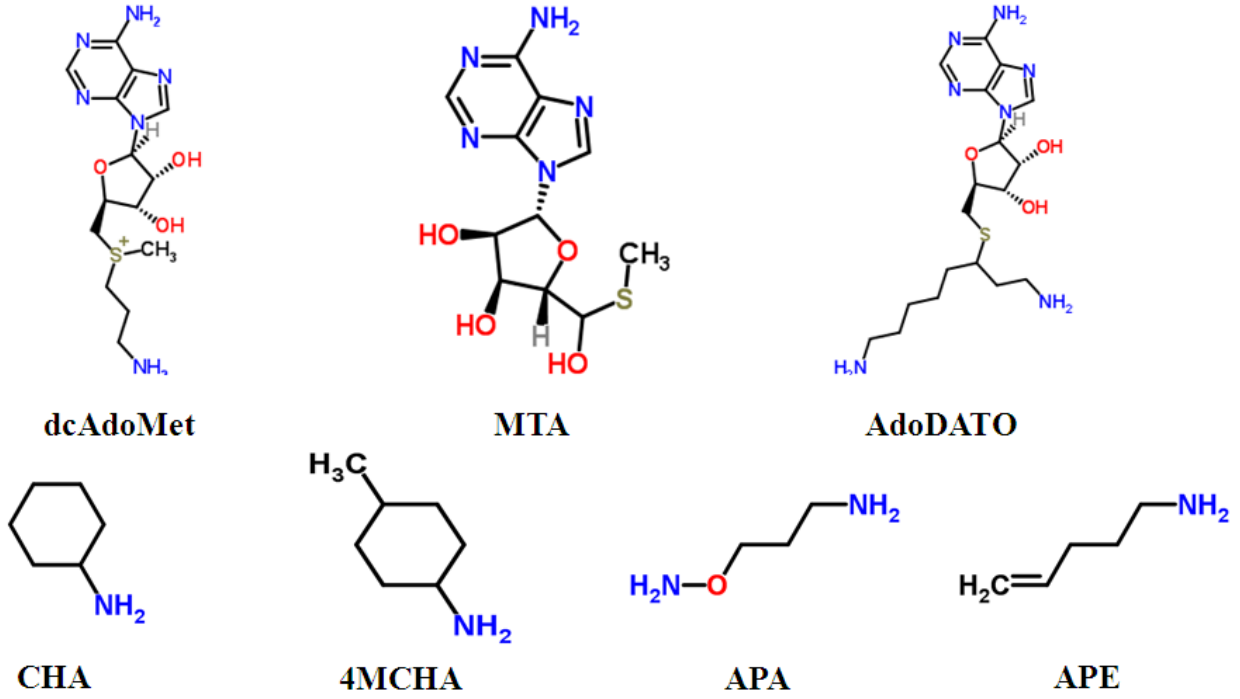

Figure 4.1: Chemical structures of various SpdS inhibitors.
Chemical structures were obtained from ChemSpider (http://www.chemspider.com/) where oxygen and hydroxyl groups are shown in red and nitrogen and amine groups are in blue. Abbreviations: AdoDATO, *S*-adenosyl-1,8-diamino-3-thio-octane; APA, 3-aminooxy-1-aminopropane; APE, 5-amino-1-pentene; CHA, cyclohexylamine; dcAdoMet, decarboxylated *S*-adenosyl-L-methionine; 4MCHA, *trans*-4-methylcyclohexyl amine; MTA, 5'-methylthioadenosine.

Despite the release of the *Pf*SpdS crystal structure, studies directed at polyamine biosynthesis as a drug target in *P. falciparum* have mainly been focused on *Pf*AdoMetDC and *Pf*ODC with attention only being paid to *Pf*SpdS in the last couple of years. Simultaneous targeting of these enzymes may also present a promising strategy in which to deplete polyamine biosynthesis within the parasite. In addition, since *Pf*SpdS is expressed during erythrocytic schizogony with both the mRNA and protein levels peaking at the late trophozoite stage [98], which coincides with the transcriptional abundance of the bifunctional *PfAdometdc/Odc* (Figure 1.7), simultaneous inhibition of all of the polyamine biosynthetic enzymes could take place during the same stage of the life cycle. Further studies are therefore needed to identify novel inhibitory compounds that can be used to explore *Pf*SpdS as a potential drug target for the chemotherapeutic treatment of malaria parasites.

The active site of SpdS contains two binding cavities, one for the adenosine substrate dcAdoMet and the other for the diamine putrescine. Early spatial deductions concerning the active site of SpdS suggested that the putrescine-binding cavity has favourable hydrophobic interactions with central primary alkyl components of putrescine and other alkylamines [226]. Other requirements for inhibitory activity of putrescine cavity binding compounds appeared to be related to the

atomic length of the alkyl chain and the flanking amine groups, illustrated by the fact that inhibitors 5-amino-1-pentene (APE), 4MCHA and APA have similar alkyl chains lengths (Figure 4.1) [98]. Of these, 4MCHA is considered as the most promising *Pf*SpdS inhibitor. This cyclohexylamine-based inhibitor was shown to occupy the putrescine-binding cavity where the cyclohexyl ring and methyl group align with the methylene groups of putrescine and the amine group occupies the region of the non-attacking nitrogen of putrescine [119]. Binding of the inhibitor was shown to be extremely effective with a K_i of 0.18 µM and an IC_{50} value of 35 µM on the parasites cultured *in vitro*. However, spermidine supplementation did not reverse the effects of inhibition and the possibility of 4MCHA having non-selective inhibition could unfortunately not be excluded [98]. Continuous *in vivo* administration of 4MCHA only reduced body-weight gain in rats and resulted in non-lethal altered spermine content in various tissues [228]. The inhibitor also had no effect on parasite proliferation *in vivo* and failed to cure *P. berghei*-infected mice [93], possibly due to assimilation of 4MCHA in the host organism. Extensive structure-activity relationship studies of this compound did not result in improved inhibitory compounds [226]. AdoDATO, resembling the dcAdoMet and putrescine transition state, has been shown to have remarkably good binding characteristics to *Pf*SpdS with an *in vitro* enzyme inhibitory activity of 8.5 µM. Subsequent X-ray co-crystallisation studies confirmed that the compound occupies both the dcAdoMet and putrescine-binding cavities [119].

Crystallographic evidence has sparked interest for the development and application of computational structure-based drug design approaches against *Pf*SpdS [119]. A study by Jacobsson *et al*. in 2008 identified several active site binders using a structure-based pharmacophore model, virtual screening and experimental validation with NMR. Two of the compounds were predicted to bind in the putrescine-binding cavity. Interestingly, these two compounds were shown to have stronger binding affinity in the presence of MTA, which could be due to the known feedback regulatory effects of MTA on *Pf*SpdS activity thereby providing additive inhibitory effects [98] or that the occupied dcAdoMet-binding site stabilises the binding of the compounds within the putrescine-binding pocket [97,119]. Several other compounds were predicted to bind in the dcAdoMet-binding cavity and were shown to compete with MTA. However, two weaknesses of this study include the treatment of the protein as a rigid body, which means that induced fit effects of compounds were not considered and several promising compounds could therefore have been missed as well as the similarity of the compounds to AdoMet. Since the binding interactions of AdoDATO were used as the search model in the pharmacophore model, many of the compounds resemble the AdoMet structure and may

therefore display off-target effects and reduced specificity due to the many important functions that AdoMet perform [178].

The lack of the discovery of effective compounds against *Pf*SpdS activity by following both ligand and receptor-based approaches warranted the need of a different approach to identify novel lead compounds. The development of a receptor-based, "dynamic" pharmacophore model (DPM) was consequently selected as the method of choice. This methodology was developed by Carlson *et al*. and attempts to account for the inherent flexibility of the active site, thereby aiming to reduce the entropic penalties associated with ligand binding [229]. The need to incorporate protein flexibility during virtual screening has been a long standing challenge and it is estimated that top docking algorithms incorrectly predict binding poses 50 to 70% of the time when a single rigid receptor structure is used [230].

In the doctoral study by P. B. Burger (University of Pretoria, [231]), a receptor-based DPM was developed to identify potential inhibitory compounds against *Pf*SpdS that could be optimised as good inhibitors of *Pf*SpdS [231]. The results from this study form the basis of this chapter in which the compounds that were identified were validated with the use of protein X-ray crystallography.

4.1.1. Identification of novel compounds against *Pf*SpdS with the use of a dynamic pharmacophore model

At the start of this study, several *Pf*SpdS structures had been deposited in the PDB database and therefore provided valuable starting points to develop a novel, receptor-based DPM for *Pf*SpdS. An area of 7 $Å^2$ containing 62 residues of the *Pf*SpdS active site co-crystallised with AdoDATO (2I7C, chain C) was used to create a subensemble, which was subsequently used in a MD simulation. This approach ensured a better sampling of the active site conformational changes than using a rigid protein backbone [229]. The clustering was performed separately for each monomer of the simulated dimer and the centre structures of the top five representative clusters of both monomers were selected and compared based on their root mean square deviation (RMSD) values. From these structures five structures were selected to best represent the RMSD range between the structures and were subsequently used in further studies (Figure 4.2). These selected structures were representative of 96.2% of the sampled phase space and should therefore be statistically more meaningful than randomly selected structures from the MD simulation.

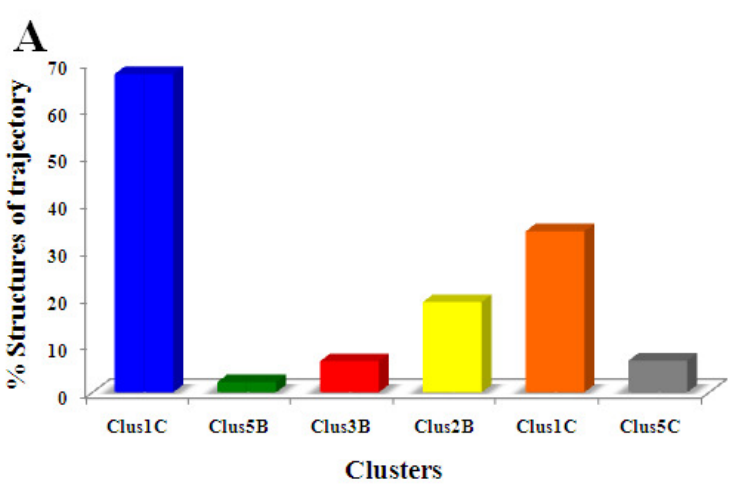

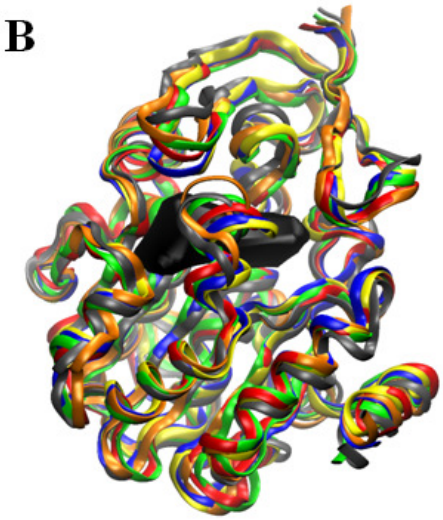

C

Structures	Clus1C	Clus5B	Clus3B	Clus2B	Clus1C	Clus5C	2PT9 (A)	2PT9 (B)	2PT9 (C)
RMSD (Backbone)	0.00	0.72	1.19	1.46	1.67	1.80	1.56	1.65	3.77
RMSD (Active site)	0.00	0.69	1.32	1.86	2.25	2.40	1.96	2.17	3.68

Figure 4.2: Clustering of the MD trajectory of *Pf*SpdS in the absence of ligands.
(A) The representative cluster sizes in percentage of total structures sampled for both monomers B and C of the structures selected to represent the *Pf*SpdS subensemble (i.e. Cluster 1 of monomer B (Clus1B) represents 68% of the total structures sampled for monomer B). (B) The representative structure ensemble obtained during phase space sampling of *Pf*SpdS using MD. The active site surface is displayed in black. (C) The RMSD values of both the backbone and active site residues of the substructure ensemble. The RMSD values of the crystal structure of *Pf*SpdS (2PT9 monomers A to C) are also included.

A comparison between the MD starting structure and the subensemble of structures revealed important conformational changes within the putrescine-binding cavity. Most significant is the conformational change that residue Gln229 undergoes in the absence of AdoDATO. The amide group of this residue orientates itself perpendicular in the apo-state compared to the orientation within the holo-state, which was later confirmed by the release of the apo-*Pf*SpdS crystal structure (2PSS). The adopted orientation of Gln229 would not allow for the identification of pharmacophore features (PhFs) that represent binding of the attacking nitrogen of putrescine. Therefore, although the conformation of Gln229 adopted during the MD simulation was confirmed by the apo-*Pf*SpdS structure, it was clear that using only the subensemble of structures for the development of a DPM would not adequately represent the binding characteristics of the active site and in particular the putrescine-binding cavity. Subsequently, the three monomers of *Pf*SpdS co-crystallised with 4MCHA and dcAdoMet (2PT9) were included in the negative image construction of the *Pf*SpdS active site. It was concluded that these structures provided adequate phase space sampling for both the bound- and apo-states.

The chemical space within the active site was subsequently explored using molecular interaction field (MIF) analysis to find energetically favourable binding hotspots by using probes representing hydrogen bond donor (HBD), hydrogen bond acceptor (HBA) and hydrophobic (HYD) pharmacophore features (PhFs). Visual inspection of the active site of the *Pf*SpdS crystal structures 2I7C and 2PT9 containing AdoDATO and 4MCHA, respectively, revealed two solvent molecules that make important interactions with their respective PhFs (residues Glu231 and Glu46) [119]. A water probe was therefore used to identify these binding hotspots for the water molecules within the subensemble of structures. These water molecules therefore facilitate PhF identification by providing important HBD and HBA characteristics within the binding areas of interest. The most common chemical moieties were found to be the NH, OH, CH_2 and NH_3^+ entities and were subsequently considered in the selection of probes to explore the *Pf*SpdS active site.

As mentioned before, the active site of *Pf*SpdS is divided into two binding cavities, one for putrescine and one for dcAdoMet. The r-shaped cavity of the active site and its dimensions led to the subdivision of the entire active site into four binding regions, namely DPM1 through to DPM4, to facilitate the pharmacophore searches as well as to explore specific regions of interest within the protein (Figure 4.3). For each of these regions various DPMs represented by different combinations of PhFs were constructed. Figure 4.3A shows a 2D representation of the *Pf*SpdS active site with the natural occurring substrates within their respective binding cavities.

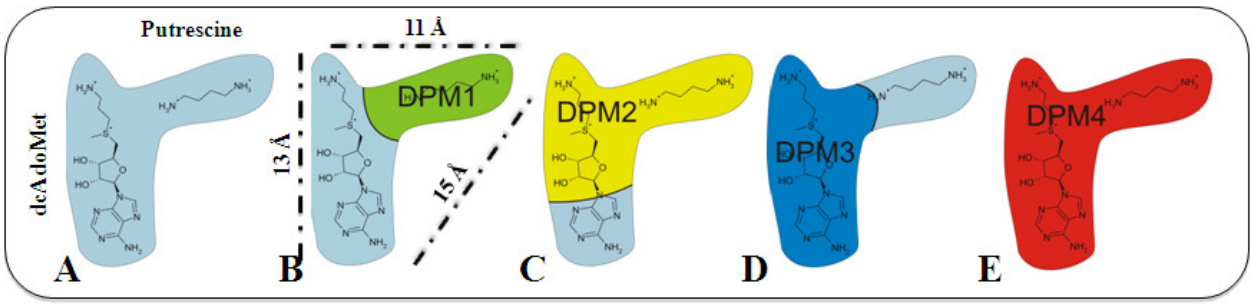

Figure 4.3: 2D representation of the active site of *Pf*SpdS illustrating different regions used to explore and construct DPMs.
(A) The *Pf*SpdS active site containing the natural occurring substrates dcAdoMet and putrescine within their respective binding cavities. (B) to (E) DPMs 1 to 4. The distances in Å between the furthest apart HBD PhFs within the entire binding cavity are shown in (B).

The DPM1 binding region was selected to explore the putrescine-binding cavity (Figure 4.3B, green). DPM2 was selected to explore the chemical space extending from the putrescine-binding cavity into the dcAdoMet-binding cavity by bridging of the catalytic centre (Figure 4.3C, yellow). DPM3 included the catalytic centre and was used to explore the dcAdoMet-binding

cavity (Figure 4.3D, dark blue) while DPM4 was used to explore the entire active site of *Pf*SpdS (Figure 4.3E, red).

The drug-like subset of the ZINC database containing 2 011 000 unique entries was screened for compounds using the DPMs. The compounds identified during these searches were fitted to their corresponding DPM to obtain the best fitting compounds and these were ranked accordingly. Visual inspection of these compounds was then performed to select the top compounds based on their fit values and orientation within the active site. Selected compounds were finally docked using AutoDock 4 [232] to evaluate their energy scores and poses within the active site. Representative compounds were selected for the four DPMs to test *in vitro* against the recombinant enzyme but only one of the nine compounds, which targets the DPM2 binding cavity, showed significant inhibitory activity and will therefore be discussed here.

4.1.1.1. Identification of compounds targeting the DPM2 binding cavity

Besides for AdoDATO that occupies the entire active site, there are currently no inhibitors that bind within the DPM2 cavity, which involves the catalytic centre. PhFs within this cavity were specifically selected (Figure 4.4A) and fourteen DPMs were constructed. The ZINC database screen resulted in 1800 hits for which the best-fit values were calculated and subsequently used in combination with visual inspection as selection criteria. Twenty-four compounds were selected and docked to evaluate the docking poses and related docking energies before they were considered for *in vitro* testing.

The compound *N*-(3-aminopropyl)-*trans*-cyclohexane-1,4-diamine (NACD) was rationally derived by taking into consideration the information obtained from MIF analysis as well as confirmed PhFs (protein-ligand interactions) and represents a basic structure or scaffold for an inhibitor of *Pf*SpdS, which is similar in structure to spermidine (Figure 4.4B). NACD is not commercially available but has been tested for inhibition against deoxyhypusine synthase and found not to inhibit the latter [233]. NACD was docked to *Pf*SpdS resulting in the expected binding poses with good binding energies. The cyclohexylamine ring of NACD would bind in a similar manner as 4MCHA does while the aminopropyl chain would bind to the same cavity as the aminopropyl group of dcAdoMet (Figure 4.4B). It is also expected that the hydrogen bonds between the nitrogen connecting the aminopropyl chain of NACD to the cyclohexylamine ring would reduce the binding penalty an aliphatic carbon would have by bridging the catalytic centre and thus increase the binding affinity and inhibition.

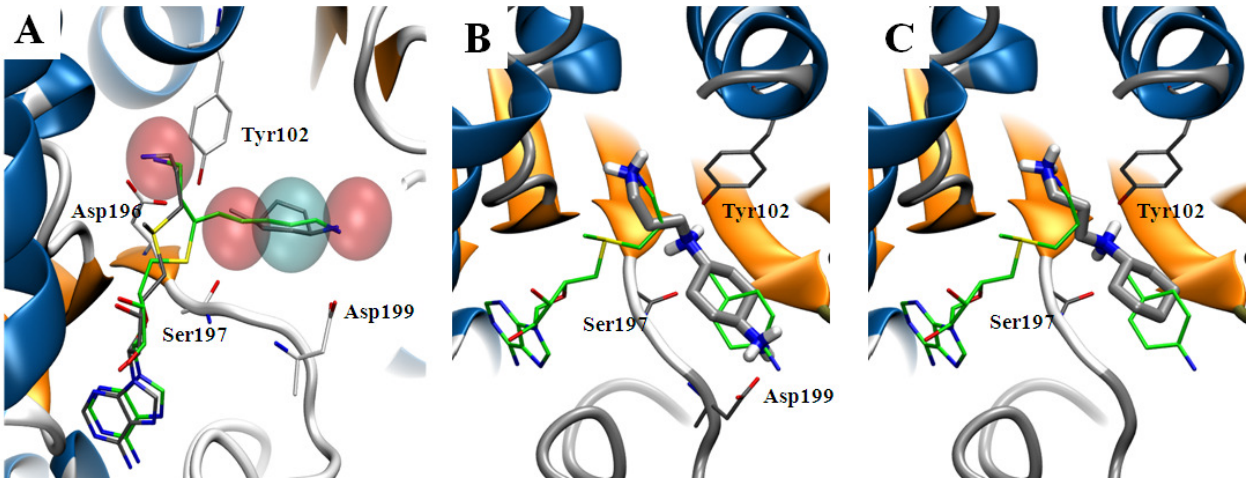

Figure 4.4: PhFs selected to describe the most important binding characteristics of the DPM2 binding cavity as well as the proposed docking poses of NAC and NACD within *Pf*SpdS.
(A) The PhFs best describing the binding characteristics of the DPM2 binding cavity within *Pf*SpdS. The red spheres represent the positive ionisable features and the blue sphere represents the hydrophobic feature. AdoDATO is shown in green and 4MCHA and dcAdoMet are shown in grey. The residues in white represent some of the residues that define the PhFs shown. (B) The docking pose of NACD (grey). Hydrogen bonds are predicted to form with Ser197 and Tyr102 upon binding. The aminopropyl chain of NACD bridges the catalytic centre and binds within a similar chemical space as the aminopropyl chain of dcAdoMet. 4MCHA and dcAdoMet are shown in green. (C) The docking pose of NAC (grey). NACD only differs in the additional amino group on the cyclohexyl ring, which is predicted to form a hydrogen bond with Asp199 that forms part of the gate-keeping loop (grey ribbon). 4MCHA and dcAdoMet are shown in green.

However, since NACD was not commercially available at the time, substructure searches using SciFinder were performed to identify similar compounds. *N*-(3-aminopropyl)-cyclohexylamine (NAC) was subsequently identified and was docked to *Pf*SpdS to evaluate its binding pose and docking energies. Good binding poses and low binding energies were obtained. NAC differs from NACD in that its ring moiety is a cyclohexylamine and not a 1,4-diaminocyclohexyl ring and therefore assumes the same binding pose and hydrogen bond pattern as NACD except for the missing amino group (Figures 4.4B and C). This made NAC a good alternative to test.

In this study we report the evaluation of two lead inhibitory compounds against *Pf*SpdS that were identified *in silico* with the use of a dynamic DPM with the aim of further chemical optimisation to promote these to potential antimalarial therapeutics. These hits were tested against the recombinant *Pf*SpdS protein followed by the kinetics of inhibition. These compounds were furthermore tested for their effect on the survival of *in vitro* cultured malaria parasites. Finally, protein crystallography was performed to validate the *in silico* predicted interactions of these compounds within the active site of the protein. Besides for the large AdoDATO complex, this is the first study that has identified an inhibitory compound that crosses the catalytic centre of the *Pf*SpdS active site and thereby competes with putrescine and dcAdoMet binding.

4.2. Methods

4.2.1. Enzyme kinetics of *Pf*SpdS treated with lead inhibitor compounds

These studies were performed by S.B. Reeksting [101]. A 87 bp N-terminus deletion of *PfSpds* cloned into pTRCHisB (Invitrogen) was expressed and purified from *E. coli* BLR (DE3) according to Haider *et al*. [98]. Purified *Pf*SpdS was subsequently assayed and the spermidine reaction product was visualised and quantified using thin layer chromatography and liquid scintillation counting as described previously [98]. Statistical analysis was performed using paired Students t-test with GraphPad Prism v5.0 (GraphPad Software, Inc.) in which *P*-values below 0.01 were considered statistically significant.

Additional kinetic experiments were performed to determine the K_i of NAC (TCI Europe, 251 g/mol) by varying the putrescine concentrations and keeping the concentration of dcAdoMet fixed at 100 µM. Reaction incubation and enzyme inactivation was performed as before.

4.2.2. *In vitro* growth inhibition of *P. falciparum*

These studies were performed by D. Le Roux [234]. *P. falciparum* strain 3D7 was maintained as described in the method of Trager and Jensen [235]. Parasites were synchronised with D-sorbitol (Sigma-Aldrich) according to established methods [236]. *In vitro* growth inhibition was monitored with the Malaria SYBR Green I Fluorescence assay [237,238]. The binding of SYBR® Green I (Invitrogen) to parasitic nucleic acids during the ring stage of parasite growth (1% parasitaemia, 2% haematocrit) was monitored at the end of a 96 h incubation period at 37°C. NAC and NACD (PharmaAdvance Inc, China, 280.61 g/mol) were selected for IC_{50} determination. NAC was dissolved in dddH_2O and NACD in 1xPBS and the compounds were diluted two-fold from starting concentrations of 1 mM and 600 µM in culture medium. Treated and untreated parasites were run in parallel and all assays were performed in triplicate in 96-well micro titre plates. A volume of 0.2 µl of SYBR Green I/ml of lysis buffer (20 mM Tris/HCl pH 7.5, 5 mM EDTA, 0.008% (w/v) Saponin, 0.08% (v/v) Triton X-100) was added to each well followed by gentle mixing. After 1 h of incubation in the dark at RT, fluorescence was measured with a Flouroscan Ascent FL Fluorimeter 2.4 with excitation and emission wavelengths of 490 nm and 520 nm, respectively and an integration time of 1000 ms.

Analysis of the fluorescence obtained was performed with SigmaPlot v11.0. Fluorescence readings were plotted against the logarithm of the compound concentration to produce a sigmoidal dose response curve. Curve fitting by non-linear regression was performed to yield the

IC_{50} values, which represent the concentrations that produced 50% of the observed decline from the maximum counts in the untreated control wells.

4.2.3. Near-UV CD of *Pf*SpdS in the presence of active site ligands

Near-UV CD was performed to test whether any structural changes take place when the active site is occupied by substrates or the NAC and NACD inhibitors. The results could also be used to validate possible structural changes observed with the protein co-crystallised with the inhibitors. Previous results have shown that binding of dcAdoMet or MTA stabilise the active site gate-keeping loop, which contains residues DSSDDPIGPAETLFNQN. The JASCO J815 CD instrument was used to determine the near-UV spectra of the purified *Pf*SpdS protein at a concentration of 1 mg/ml (28.9 µM) in crystal buffer (10 mM HEPES pH7.5, 500 mM NaCl). The protein samples were incubated at RT for 30 min with [2.5 mM NAC] or [2.5 mM NACD], [2.5 mM putrescine], [20 µM dcAdoMet+2.5 mM spermidine] and [20 µM dcAdoMet]. The low amount of dcAdoMet relative to the protein concentration (20 µM versus 29.8 µM) that was used due to limited quantities of this compound could mean that possible structural changes as a result of dcAdoMet binding would not be detected. As control, the spectrum of the apo-protein was also measured. Measurements were conducted in 10 mm cuvettes at a wavelength range of 320 to 250 nm at 20°C, using a wavelength interval of 0.5 nm, a bandwidth of 1 nm and a scanning speed of 20 nm/min. Five readings were accumulated per sample, the spectrum of crystal buffer was subtracted and the data points were averaged.

Since near-UV CD gives a much weaker signal than far-UV CD double the amount of protein was used (1 mg/ml) than before (section 3.2.6) as well as a cuvette with a longer path length (10 mm versus 1 mm). The molar ellipticity ($[\theta]_M$) of each data point in units deg cm^2 $dmol^{-1}$ was calculated as follows according to Bale *et al*. [185]:

$$[\theta]_M = \frac{\Delta\theta \times MW}{10 \times l \times C}$$

Where $\Delta\theta$ is the reading in degree, MW is the molecular weight of the protein in g/mol, l is the path length in cm and C is the concentration of the protein in mg/ml.

Signals that arise in the region from 250-270 nm are attributable to Phe, signals from 270-290 nm are from Tyr and those from 280-300 nm are from Trp. Disulphide bonds give rise to broad weak signals throughout the spectrum.

4.2.4. Protein crystallisation of *Pf*SpdS in complex with lead inhibitor compounds

4.2.4.1. Protein purification

For protein crystallisation of *Pf*SpdS, the gene sequence corresponding to a protein lacking 39 residues at the N-terminus and cloned into the p15-TEV-LIC vector was obtained from the Structural Genomics Consortium in Toronto (http://www.sgc.utoronto.ca/). Protein expression and isolation was followed according to Dufe *et al*. and included purification via both anion exchange (aIEX) and SEC [119]. Briefly, clear cell lysate after cell disruption and ultracentrifugation was loaded onto a DEAE Sepharose column (GE Healthcare) previously activated with 2.5 M NaCl and equilibrated with binding buffer (50 mM HEPES pH 7.5, 500 mM NaCl, 5 mM imidazole, 5% (v/v) glycerol). The column was washed with 20 ml binding buffer and the flow-through was collected in 0.5 ml fractions at a flow rate of 0.5 ml/min. The sizes of the proteins within the fractions that gave rise to large protein peaks at an absorbency of 280 nm were analysed with SDS-PAGE to identify the monomeric *Pf*SpdS with a size of ~30 kDa. These fractions were then combined and loaded onto a 2 ml Ni-NTA column (Sigma-Aldrich), pre-equilibrated with binding buffer. The beads were subsequently washed with 200 ml wash buffer (50 mM HEPES pH 7.5, 500 mM NaCl, 30 mM imidazole, 5% glycerol) followed by protein elution with 15 ml elution buffer (50 mM HEPES pH 7.5, 500 mM NaCl, 250 mM imidazole, 5% glycerol). A final concentration of 1 mM EDTA was added to the eluate followed by 5 mM DTT approximately 15 min later. The eluate was concentrated using a 15 ml Amicon Ultra centrifugal filter device (MWCO 3000, Millipore) to a volume of 1 ml. The concentrated protein was subsequently loaded onto a Superdex®-S200 10/300 GL SE column (Tricorn, GE Healthcare) connected to an Äkta Prime System (Amersham Pharmacia Biotech) pre-equilibrated with crystal buffer at a flow rate of 0.5 ml/min and 0.5 ml fractions corresponding to the homodimeric ~60 kDa protein were collected.

His-tag cleavage with 500 U ProTEV protease (Promega) was performed overnight at 4°C in the presence of 1 mM DTT. ProTEV protease contains an N-terminal HQ-tag (HQHQHQ, Promega) such that, together with the cleaved His-tag from the recombinant *Pf*SpdS protein, it can be removed from the reaction by incubating it with a metal-affinity resin. The *Pf*SpdS protein without the His-tag was therefore purified via a second Ni-NTA purification by collection of the flow-through. The column was washed with an additional 10 ml of binding buffer and the eluates were combined. The ProTEV and cleaved His-tag was subsequently eluted with elution buffer. Cleavage of the His-tag was confirmed with Western immunodetection using 1:2500 HisProbe™-HRP (Pierce Biotechnology) and 1:2500 of polyclonal *Pf*SpdS antiserum, which

was raised in rabbits. For the latter Western blot goat anti-rabbit IgG-HRP was used as secondary antibody. Western blotting was then performed as stipulated in section 2.2.6. Finally, buffer exchange was performed in crystal buffer with a centrifugal filter to a protein concentration of 22.8 mg/ml and stored at 4°C.

4.2.4.2. Protein crystallisation

Purified *Pf*SpdS was crystallised in the presence of NACD, MTA and NAC using the hanging drop vapour diffusion method at 293 K. Protein solution was mixed with reservoir solution containing 25% (w/v) PEG3350 (Sigma-Aldrich), 0.1 M MES pH 5.6 and 0.1 M $(NH_4)_2SO_4$. The *Pf*SpdS-NACD complex was obtained by using 10 mg/ml protein pre-incubated with 2.5 mM NACD for 30 min at RT before mixing 1 µl with 2 µl reservoir solution. The *Pf*SpdS-NACD-MTA complex was obtained with pre-incubation of 5 mg/ml protein with 2.5 mM of both NACD and MTA followed by mixing 1 µl with 1 µl of reservoir solution while 10 mg/ml protein was used at the same ratio for the *Pf*SpdS-NAC-MTA complex.

Prior to data collection, crystals were transferred to cryo protectant solution containing the reservoir solution and 15% glycerol before being flash frozen in a liquid nitrogen stream at 100 K. Data was collected at beam line I911-2 (MAX-lab, Lund, Sweden) and processed using the XDS package [239].

Molecular replacement was performed with CNS v1.2 [240,241] using apo-*Pf*SpdS (2PSS) as template for *Pf*SpdS-NACD and *Pf*SpdS-MTA (2HTE) for both *Pf*SpdS-NACD-MTA and NAC-MTA. The programmes Coot, CNS v1.2 [240,241] and CCP4 [242] were used for model building and refinement. The library files for NAC and NACD were generated using the PRODRG server [243]. The electron density maps were visualised to localise the traces of the polypeptide chains in the molecular graphics programme COOT. Model refinement was then performed with refmac v5.5 (CCP4 v6.1.13) [242,244] and CNS v1.2 followed by the manual adjustment of residues according to several geometrical constraints and also for improved fitting of atoms within their respective densities. The updated coordinate files were then used to calculate improved electron density maps, which was followed by another cycle of model building. With each iterative cycle of model building, map generation and model refinement, the side chains became correctly assigned with acceptable peptide geometries (bond lengths and angles) and side chain rotamers.

The main chain polypeptide conformations of the crystal structures were verified by Ramachandran plots [245] with the programme RAMPAGE [246]. In these plots the dihedral peptide angles phi (φ) and psi (ψ) are plotted for each residue (i.e. for each residue in all of the monomeric chains that are solved), and the positions of these data points should then lie in the allowed regions of φ and ψ angles that correspond to energetically acceptable protein secondary structures [247]. The goal is to obtain a structure in which all the solved residues lie within the favoured or at least allowed regions except for Gly residues, which are not restricted by φ and ψ angles and may therefore be located at any position.

Model quality was evaluated with PROCHECK (Appendices I, II, III) [153] and the Joint Structural Genomics Consortium (JCSG) Quality Control v2.7 (http://smb.slac.stanford.edu /jcsg/QC/), which contains MolProbity (http://molprobity.biochem.duke.edu/) [248] and ADIT (http://deposit.pdb.org/validate/) checks.

4.3. Results

4.3.1. Enzyme kinetics and *in vitro* parasite treatment of novel inhibitory compounds against *Pf*SpdS

In vitro testing of NAC at a 100 µM concentration showed a remarkable 86% reduction in *Pf*SpdS activity, which warranted further investigation of this compound. Enzyme kinetics was subsequently performed for the compound and the K_i value was determined (Figure 4.5A). Data from a Lineweaver-Burk extrapolation indicated a similar K_m value for putrescine at 25.1±3.2 µM and a slightly lowered V_{max} value at 96.4±2.7 µmol/min/mg than previously reported [98]. Additionally, in the presence of NAC the K_m and V_{max} parameters of *Pf*SpdS were affected. For NAC to be a true competitive inhibitor of the putrescine-binding site, only the K_m value is expected to change. However, the kinetic data showed that the V_{max} was not re-established at putrescine concentrations far greater than its K_m, suggesting that NAC also affected the binding of the second substrate, dcAdoMet and that the additional putrescine was not able to disrupt the tight binding interaction of NAC. A secondary plot from the Lineweaver-Burk plot was used to calculate the K_i value of NAC, which was found to be 2.8 µM (Figure 4.5B). Inhibition kinetics with NACD was unfortunately not performed due to the compound not being commercially available at the time of recombinant protein testing.

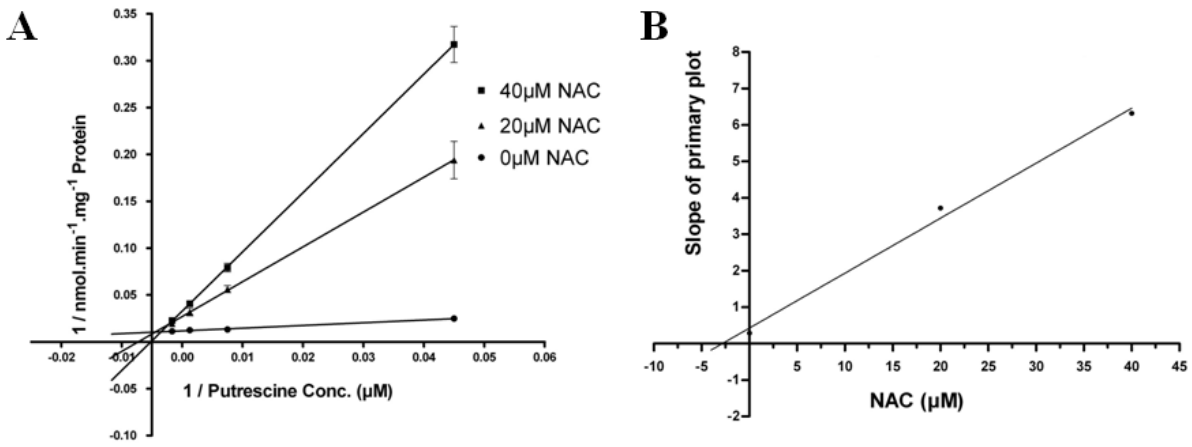

Figure 4.5: Inhibition kinetics of *Pf*SpdS treated with NAC.
(A) Lineweaver-Burk plot and (B) secondary Lineweaver-Burk plot of the slopes obtained from the plot in (A) versus inhibitor concentration to determine K_i. Results are the mean of five independent experiments ±S.E.M.

Furthermore, the ability of compounds NAC and NACD to inhibit the growth of *P. falciparum* parasites cultured *in vitro* was determined using standard growth inhibition assays. Subsequent IC_{50} determinations showed that NAC has an inhibitory activity of 105±13 µM (n=5) while that of NACD is slightly more effective at 81.2±13 µM (n=7) (Figures 4.6A and B). The physiological effects of the inhibitors on parasite growth were also investigated via the treatment of the parasite cultures with 2xIC_{50} concentrations of each inhibitor immediately following the infection stage. Parasite morphology showed changes at 72 h post-treatment with NAC whereas changes were observed as soon as 48 h post-treatment with NACD [234]. Treatment also resulted in delayed cell cycle progression compared to the untreated culture. Furthermore, co-treatment of either NAC or NACD with the AdoMetDC inhibitor MDL73811 or ODC inhibitor DFMO showed additive inhibition [234]. These results indicate that the simultaneous inhibition of *Pf*ODC and *Pf*SpdS could result in a polyamine depleted state within the parasites.

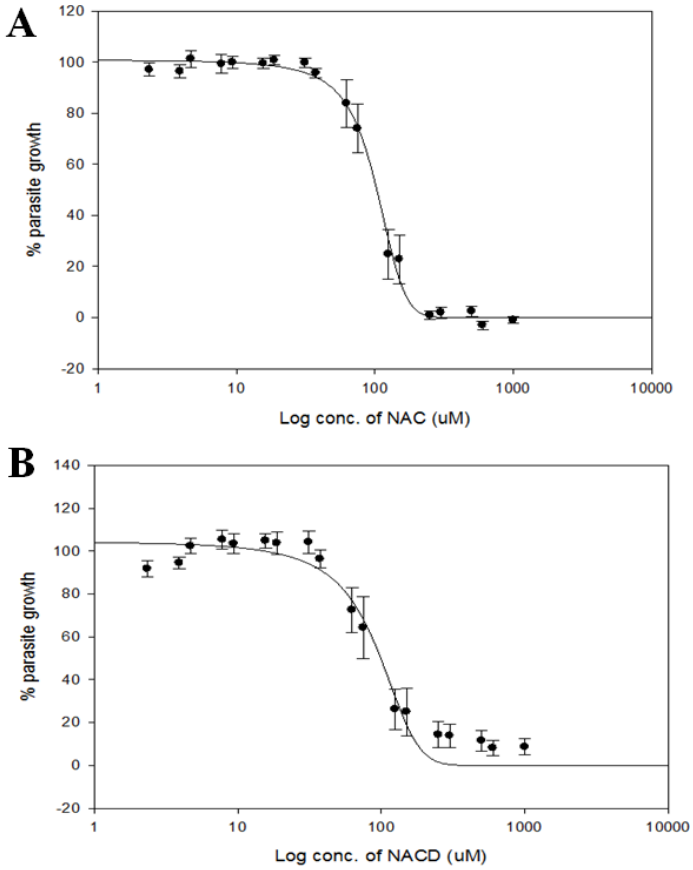

Figure 4.6: Dose response curves of *P. falciparum* cultures treated with NAC (A) and NACD (B) for determination of IC_{50} values.
Results are shown as S.E.M and were obtained from five individual experiments for NACD (n=5) and seven experiments for NACD (n=7), performed in triplicate.

Based on the *in vitro* results it is anticipated that, compared to NAC, the inhibition efficiency of NACD on the recombinant protein would be more effective, since the extra amine group on the cyclohexyl moiety is predicted to stabilise inhibitor binding within the active site via interaction with Asp199. Subsequently, the *in silico* predicted binding interactions of the lead inhibitor compounds were validated with the use of X-ray crystallography of the protein in complex with these compounds.

4.3.2. Preparation of high yields of pure *Pf*SpdS for protein crystallography

Large-scale expression of *Pf*SpdS for crystallisation studies was obtained from 2.5 liters of bacterial culture followed by protein purification involving aIEX, batch purification with Ni-NTA resin and SEC. aIEX analyses of the total soluble lysate collected after cell disruption and ultracentrifugation showed the elution of four major peaks corresponding to fractions #7 (V_e 5 ml), #17 (10 ml), #21 (11.8 ml), #26 (14.2 ml) (Figure 4.7A). *Pf*SpdS consists of 283 residues and has a pI of 6.18. The presence of *Pf*SpdS within these fractions was confirmed with SDS-PAGE with an expected monomeric protein size of ~31 kDa under denaturing conditions.

The SDS-PAGE results showed the presence of a protein ~31 kDa in size in fractions #17 and #21, with a small amount in #26 (Figure 4.7B), which could correspond to the monomeric *Pf*SpdS protein under the denaturing SDS-PAGE conditions. Several contaminating proteins were also present within the collected samples to be removed during the secondary and tertiary purification steps. Fractions 12-24 were pooled and concentrated for subsequent affinity chromatography using Ni-NTA resin. The 5 mM imidazole within the binding buffer should not interfere with His-tag binding and was therefore not removed prior to column loading.

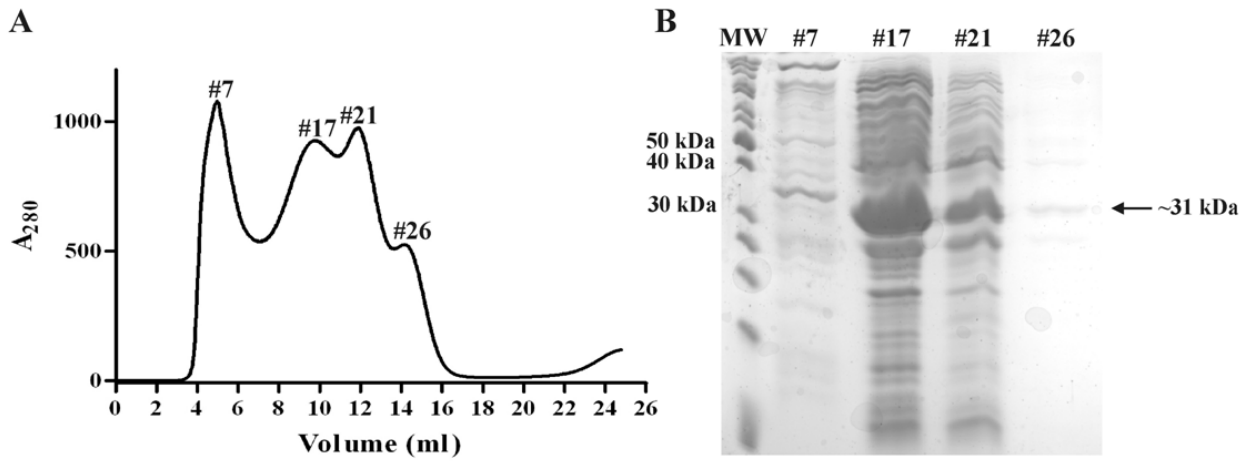

Figure 4.7: The aIEX chromatogram (A) and subsequent SDS-PAGE analysis (B) of the *Pf*SpdS fractions. MW: PageRuler Unstained Protein Ladder; #7, #17, #21, #26: fractions collected with aIEX. The expected size of the monomeric *Pf*SpdS protein is shown.

The His-tagged *Pf*SpdS sample eluted from the Ni-NTA resin in 15 ml elution buffer was further purified by separation with SEC. The results showed the presence of a major protein peak at a V_e of 16.3 ml (Figure 4.8A), indicating the successful removal of the untagged, contaminating proteins as seen in Figure 4.7B during the washing step of affinity chromatography. The protein peak corresponds to a calculated size of the ~60 kDa homodimer and fractions 13-18 were collected and pooled (Figure 4.8). Denaturing SDS-PAGE analyses of the affinity and SE chromatography-purified proteins showed the presence of the pure monomeric *Pf*SpdS protein at ~31 kDa. A small amount of protein ~70 kDa in size could represent *E. coli* Hsp70, a protein that often co-purifies during plasmodial proteins expression in *E. coli*, but still needs to be verified with MS.

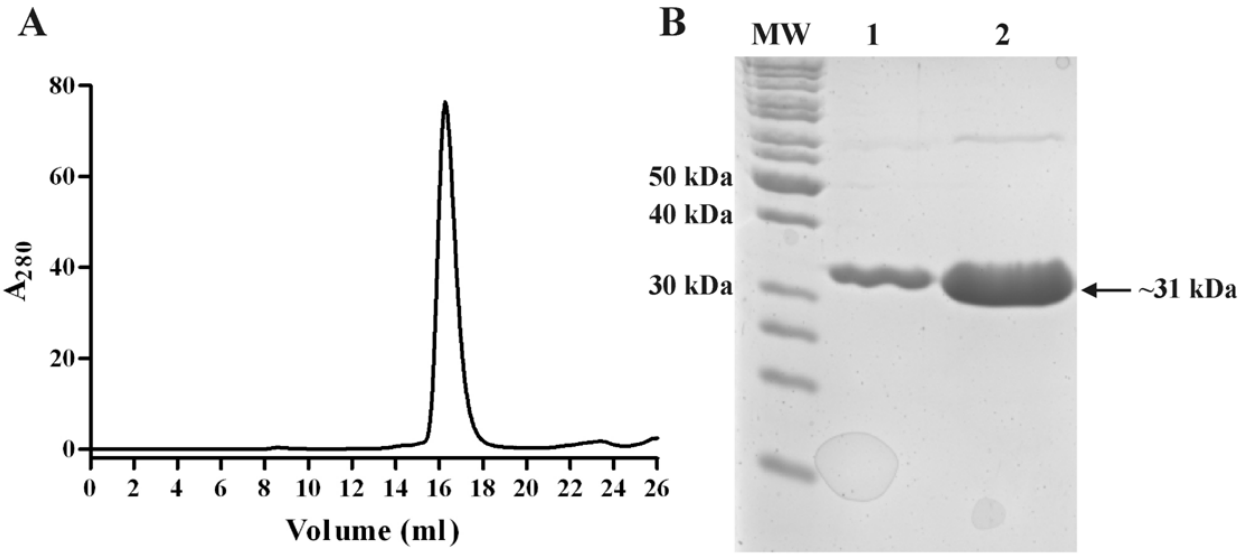

Figure 4.8: SEC of affinity-purified *Pf*SpdS (A) followed by SDS-PAGE analysis (B).
(A) The protein sample eluted with affinity chromatography and the concentrated pooled fractions obtained from SEC are shown in lanes 1 and 2, respectively (B). MW: PageRuler Unstained Protein Ladder. The expected size of the monomeric *Pf*SpdS protein is shown.

Affinity tags such as 6xHis and Strep are short, flexible peptides and can often hamper the crystallisation process by interfering with the establishment of crystal contacts. In general it is therefore beneficial to remove these prior to crystallisation screens with the use of proteases that cleave the tags at engineered protease recognition sites. In the case of *Pf*SpdS, a seven residue ProTEV cleavage site (EXXYXQG/S) is present prior to the C-terminal His-tag, which could therefore be removed with the use of the highly site-specific ProTEV enzyme. The cleavage reaction in the presence of DTT was optimised for *Pf*SpdS-His in terms of reaction temperature and duration. Subsequent Western immunodetection with both the HisProbe®-HRP (Figure 4.9A) and a polyclonal *Pf*SpdS antibody (Figure 4.9B) confirmed the absence of the His-tag in the *Pf*SpdS protein after Ni-NTA elution (lane 2).

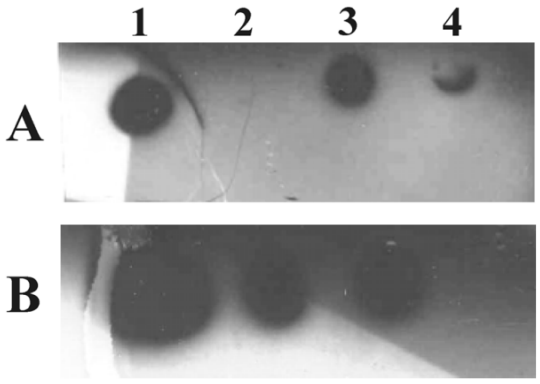

Figure 4.9: Western immunodetection of the ProTEV cleavage products collected after affinity chromatography using HisProbe®-HRP (A) and a polyclonal *Pf*SpdS antibody (B).
Lane 1: *Pf*SpdS-His collected from SEC as control of recombinantly expressed protein containing a His-tag; lane 2: flow-through of *Pf*SpdS (cleaved His-tag) collected from Ni-NTA; lane 3: eluted His-tag and Pro-TEV (containing HQ-tag) with elution buffer; lane 4: sample collected during washing of the Ni-NTA resin.

Western immunodetection confirmed the absence of the His-tag on *Pf*SpdS collected from the flow-through during Ni-NTA purification since removal of the tag prevents the protein from binding to the resin (Figures 4.9A and B, lane 2). The cleavage reaction was, however not 100% efficient, since His-tagged *Pf*SpdS protein was detected in the sample collected during the elution step (Figures 4.9B, lane 3) while the eluate probably contained cleaved His-tags, Pro-TEV protease (with HQ-tag) and *Pf*SpdS-His (Figures 4.9A, lane 3). Cleaved His-tags were also eluted during the washing step (Figures 4.9A, lane 4). The flow through collected (sample in lane 2) was finally concentrated to 22.8 mg/ml (total yield of 11.4 mg) and the protein was stored at 4°C until the crystallisation trials were performed.

4.3.3. Near-UV CD analyses of *Pf*SpdS in the presence of NAC or NACD

Prior to solving the crystal structures, the tertiary structures of *Pf*SpdS in the presence of various active site ligands were determined with near-UV CD (Figure 4.10). In this way, changes in specifically the aromatic amino acids (as an indicator of tertiary structure) and possible effects that the compounds may have on the conformation of the active site and gate-keeping loop can be observed, which can then be validated with the crystal structures. Previously it was suggested that the sulphide atom on dcAdoMet or MTA is involved in stabilisation of the loop [119] and from a drug discovery perspective it would therefore be of interest to determine the effect of NAC or NACD in the presence of MTA or dcAdoMet on this loop.

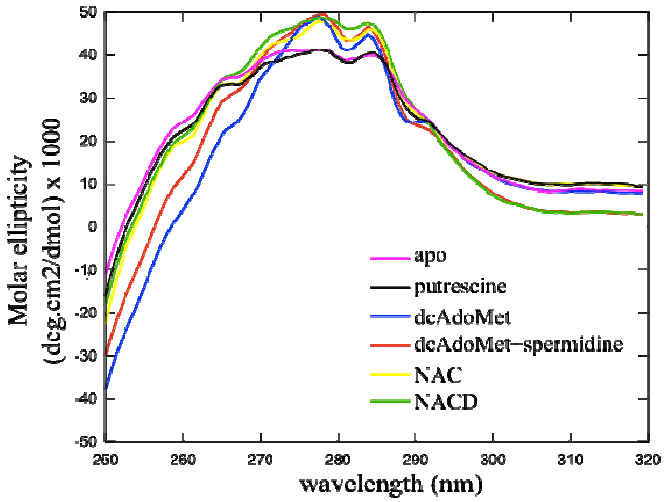

Figure 4.10: Near-UV CD analyses of *Pf*SpdS in the presence of various ligands.
The purified *Pf*SpdS protein was treated with putrescine, spermidine, dcAdoMet, NAC and NACD in different combinations and at specific concentrations and the spectra in the near-UV CD wavelength range of 250 nm to 320 nm were measured. Results are given as molar ellipticity ($[\theta]_M$) in units deg cm^2 dmol^{-1}.

The spectra of the *Pf*SpdS incubated with NAC (yellow line), NACD (green) and dcAdoMet (blue) showed remarkable similarity with no major differences therefore indicating that the

tertiary structures of these proteins are similar (Figure 4.10). Additionally, this result may indicate that binding of these ligands results in similar conformations of the active site and gate-keeping loop. On the other hand, in comparison to the spectra of the apo (Figure 4.10, pink line) and putrescine (black) samples, the ligand-bound samples show differences in terms of the signal strength and peak overlaps. The spectra of the apo and putrescine samples show high similarity and could indicate that the structures of the *Pf*SpdS protein with empty or partially filled active sites are similar. As previously suggested, the flexibility of the gate-keeping loops of these protein samples may also contribute to the observed spectra [119]. Finally, the difference in the Tyr absorption area (270-290 nm) between the apo and NAC/NACD spectra may be due to the movement of Ty264, which could be involved in the stabilisation of the cyclohexyl rings, as previously observed for 4MCHA binding [119].

4.3.4. Growth of diffraction quality *Pf*SpdS protein crystals in complex with NAC or NACD

To validate the predicted binding of NACD and NAC within the active site of *Pf*SpdS, the compounds were co-crystallised with the protein to provide atomic resolution information on the inhibitor interactions. Several manual crystal screens of the His-cleaved, pure *Pf*SpdS protein in complex with NAC, NACD and MTA were performed using the hanging drop vapour diffusion method at temperatures of 288 and 295 K. The buffer system, pH, amount of PEG3350, protein concentration and drop sizes were varied until diffraction quality crystals were obtained. All crystals grew within a couple of days at 295 K in either 2 or 3 µl drops of 5 or 10 mg/ml protein treated with 2.5 mM inhibitor in 0.1 M MES pH 5.6 precipitant solution containing 25% PEG3350 and 0.1 M $(NH_4)_2SO_4$. The crystals were shaped as three-dimensional hexagons with average dimensions of 0.1x0.3x0.06 mm (Figure 4.11). The crystal structures previously published for *Pf*SpdS were crystallised in 0.1 M BisTris pH 5.5 containing 23% PEG3350 and 0.1 M $(NH_4)_2SO_4$.

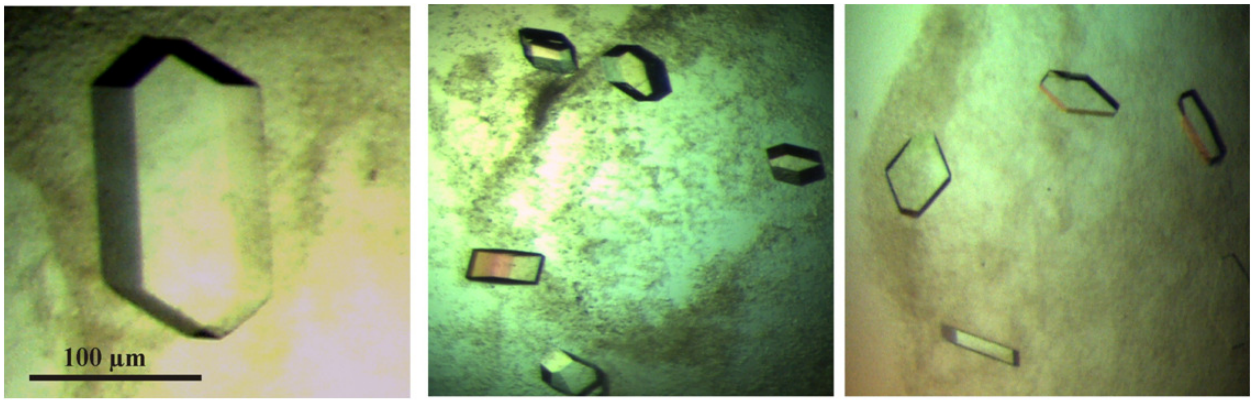

Figure 4.11: Images of *Pf*SpdS crystals in complex with NAC or NACD.
Crystals were grown at 295 K in 0.1 M MES pH 5.6 precipitant solution containing 25% PEG3350 and 0.1 M $(NH_4)_2SO_4$ with the hanging drop vapour diffusion method.

4.3.5. X-ray crystallography verifies binding of NAC and NACD in the active site of *Pf*SpdS

4.3.5.1. Crystal structure refinement results

Following crystal rotation data collection, several key steps were followed to arrive at the stage where the models could be built, these included 1) analysis of the observed reflections and positions thereof in the detector plane and optimisation of the detector distance; 2) integration of the diffraction intensities; 3) spacegroup definition and 4) correction of data followed by data scaling. Prior to the collection of the full data sets, several parameters were studied to examine the quality of data and to assign the spacegroup. The correct parameters could then be specified as required by the spacegroup in order to collect the maximum number of possible reflections. The observed diffraction patterns showed the positions of the recorded reflections for a particular plane of the crystal. The crystals were then rotated at specified angles such that exposure with X-ray could detect the remaining reflections. The XDS package was used in this study to perform these initial tasks [239].

In the case of the *Pf*SpdS-NACD crystal, two data sets were collected; firstly for the intensities in the low resolution range (1-8 Å), 200 frames were collected at an oscillation of 1° and an exposure time of 50 s after which the exposure time was decreased to 15 s for collection of 100 frames with an oscillation of 2° to collect the intensities in the high resolution range (1-2.5 Å). This strategy ensured that the intensities at low resolution were detected with the longer exposure time while overloading of the intensities at high resolution was prevented by collection of the high-resolution data with the shorter exposure time. These two data sets were then integrated separately and merged prior to reflection scaling. A single dataset was collected for *Pf*SpdS-NACD-MTA consisting of 200 frames of 20 s per frame. Although crystals for the

*Pf*SpdS-NAC complex were obtained, diffraction data could not be collected possibly due to a high degree of crystal disorder. In addition, only 132 frames were collected for the *Pf*SpdS-NAC-MTA crystal due to a problem that occurred with the cryo stream during diffraction, however with the collected data ~93% completeness in the high-resolution shell was still obtained.

The reflection files were then used to solve the phase problem, which in this study was performed by molecular replacement with published crystal structures of *Pf*SpdS as templates. These structures provided information on the phase angles and by incorporating translation and rotation functions the test and template molecules could be aligned within the asymmetric unit (ASU), such that, together with the structure factors, the models could be built with the corresponding electron density maps. The data collection and refinement statistics of the solved crystal structures are listed in Table 4.1.

The cell dimensions of the *Pf*SpdS-NACD-MTA and NACD structures are identical and data was collected in the same resolution ranges for both. The data collection for NACD-MTA was complete in the high resolution shell and provided good estimates for the quality of data scaling and averaging as given R_{meas} (Table 4.1). The latter is the multiplicity-independent factor, which means that it does not increase with an increase in redundancy (multiplicity) as R_{merge} does [249]. The multiplicity for the NACD data sets was between 4 and 5, which means that each reflection was measured 4 to 5 times during data collection, these were then averaged during data scaling to give rise to approximately 98 000 unique reflections (multiple observations of the same and symmetry-related reflections). Finally, $I/\sigma(I)$ gives an indication of the signal strength of the observed intensities and, as observed for the data here, should not be less than two (Table 4.1).

Table 4.1: Crystallography data collection and refinements statistics

	NACD-MTA	NACD	NAC-MTA
Data collection			
Space group	C121	C121	C121
Unit cell dimensions	a=196.8 Å, b=134.6 Å, c=48.5 Å, β=94.6°	a=196.80 Å, b=134.59 Å, c=48.46 Å, β=94.55	a=196.71 Å, b=134.33, c=48.33 Å, β=94.7
Molecules per asymmetric unit	3	3	3
Resolution range (Å)	20.1-1.89	20.0-1.89	19.8-2.39
No. of reflections	413846	492876	137713
No. of unique reflections	98147	98435	45723
Completeness (%) [a]	99.8 (100)	99.6 (99.8)	92.4 (94.3)
Multiplicity	4.2	5	3
R_{meas} (%) [a, b]	5.9 (41.1)	5.1 (39.8)	8 (43.6)
$I/\sigma(I)$ [a]	18.5 (3.9)	19.3 (4.1)	13.9 (4.3)
Refinement statistics			
Number of reflections	93239	93506	43435
R_{work}/R_{free} [c]	0.18/0.21	0.21/0.24	0.19/0.24
No. of atoms	7493	6780	6999
protein	6745	6481	6656
water	617	211	243
NACD	36	36	-
MTA	60	-	60
glycerol	18	18	18
1PG	17	34	17
SO_4	-	-	5
<B> (Å^2)	25.4	36.5	29.6
RMS deviations			
Bond length (Å)	0.029	0.026	0.022
Bond angles (°)	2.08	1.995	1.938
Ramachandran statistics (%) [d]			
Favoured	97.2	96.2	96.1
Allowed	99.9	100	99.9
Outliers	0.1	0	0.1

[a] The numbers in parentheses are of the highest resolution shell.

[b] $R_{meas} = (\sum_i \sqrt{\left(\frac{n_i}{n_i-1}\right)} \sum_j |I_{ij}-\langle I_i\rangle|)/(\sum_i \sum_j \langle I_i\rangle)$, the redundancy-independent factor, where n is the number of observations for reflection *i*.

[c] R_{free} is the same as R_{work}, but calculated on 5% of the data excluded from refinement. $R_{work} = (\sum |F_o-F_c|)/(\sum F_o)$, where F_o and F_c are the observed and calculated structure factor amplitudes, respectively.

[d] Ramachandran statistics were calculated using Molprobity [248].

Model refinement resulted in well defined structures such that crystallographic solvent molecules could be identified. A good indicator of model progression was given by the *R*-factor (R_{work}), which was calculated throughout the refinement steps and gave an indication of the agreement between the observed and the calculated data (Table 4.1). However, the over interpretation or over fitting of data, for example when too many solvent molecules are fitted resulting in a compensation for model errors, can result in a value that is too low regardless of the correctness of the model. The so-called R_{free} factor was therefore assessed, which used reflection data from a test set (representing 5% of the total data) that was not subjected to model refinement and therefore represented an unbiased indicator of model quality [247]. The R_{free} is therefore slightly higher than the R_{work}. For the *Pf*SpdS structures the R_{work} values were in a range that resulted in

well defined structures from which residues and solvent molecules could be clearly localised (Table 4.1).

The main chain polypeptide conformations of the crystal structures were verified by RAMPAGE-generated Ramachandran plots [245] (Figures 4.12 and 4.13) [246]. RAMPAGE uses a plot in which the borders of areas were computed by analyses of 81234 non-Gly, non-Pro, and non-pre-Pro residues with B-factors of less than 30 from 500 high resolution protein crystal structures. This resulted in a plot with sharp boundaries at the critical edges between regions as well as clear delineations between the empty areas and regions that are allowed but not favoured. The Ramachandran plot of the structure of *Pf*SpdS co-crystallised with NACD showed that no residues were located in the outlier regions (white areas) while 96.5% of the residues were positioned in the favoured regions (Figure 4.12 and Table 4.1). In addition, all Gly and Pro residues were in the favoured areas while a few pre-Pro residues were located in the allowed regions.

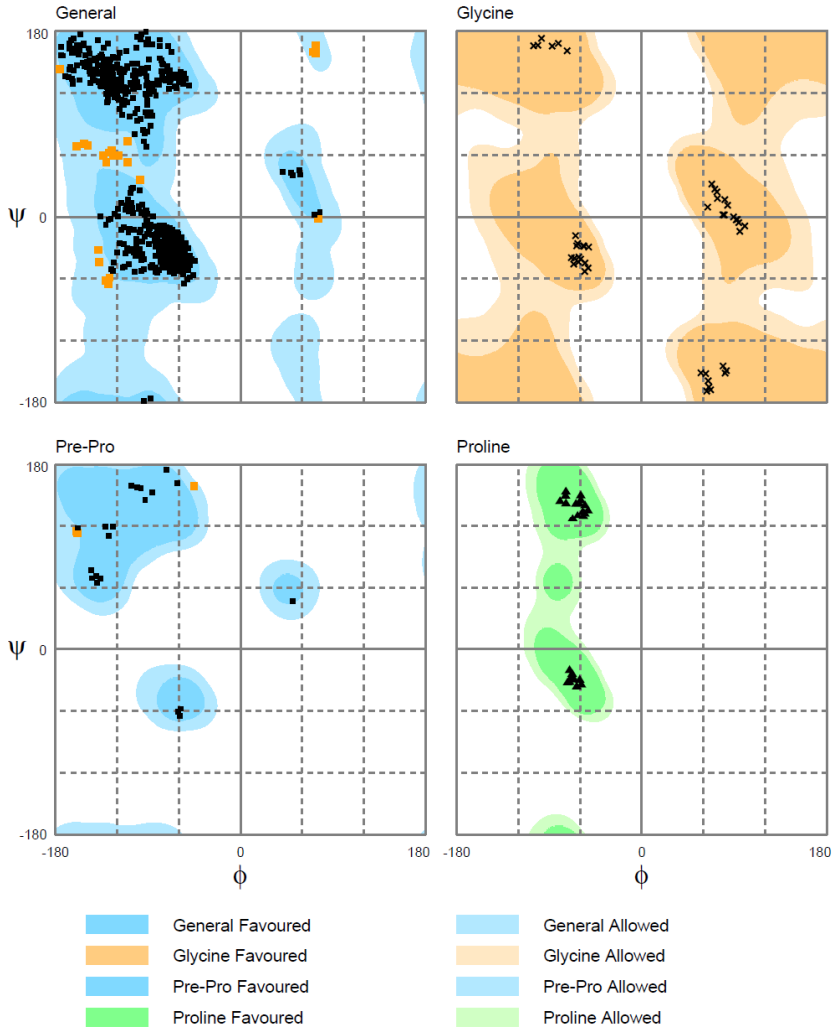

Figure 4.12: Ramachandran plot of the *Pf*SpdS-NACD structure.

For both the *Pf*SpdS-NACD-MTA and NAC-MTA structures residue Glu231 was detected as the single outlier on chain C and A, respectively. Interestingly, this residue is located within the active site and has been shown to interact with 4MCHA [119]. The observed geometric differences for this residue between the NACD and NACD-MTA/NAC-MTA structures alludes to a difference in ligand binding in the absence or presence of MTA, respectively, which will be clarified by the structures themselves. Nonetheless, the overall geometries were of high quality with >95% of the residues being in the allowed regions (Figures 4.13 and 4.14, Table 4.1).

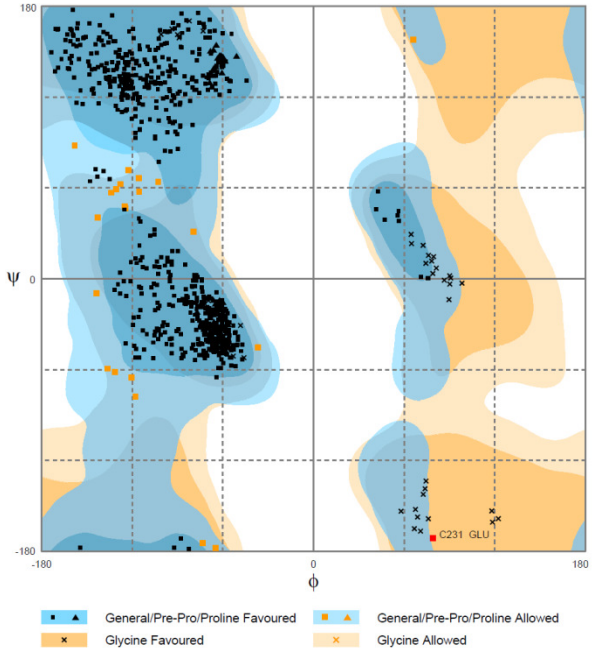

Figure 4.13: Ramachandran plot of the *Pf*SpdS-NACD-MTA crystal structure.

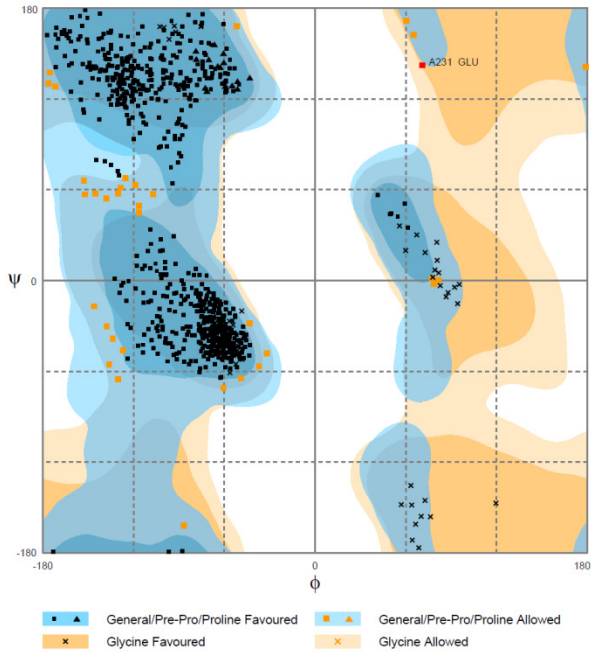

Figure 4.14: Ramachandran plot of the *Pf*SpdS-NAC-MTA crystal structure.

4.3.5.2. Overall structure of *Pf*SpdS

Crystallisation was performed with the addition of the inhibitors as well as in combination with the byproduct of the SpdS reaction, MTA. This was done as a result of previous studies that showed that inclusion of only one substrate leads to disordered gate-keeping loops [97,119]. Additionally, MTA was included since the kinetics results showed that NAC binding competes with dcAdoMet and could therefore result in a structure that does not have both the inhibitor bound within the active site and an inflexible loop (section 4.3.1).

The results of PROCHECK analyses of the three models are included in Appendices I to III. *Pf*SpdS was crystallised in space group C121 with three monomers (Matthews coefficient of 3.04) in the ASU and the solvent area occupying 50-60% of the unit cell. A representation of the crystal packing within the unit cell is shown in Figure 4.15 while the unit cell dimensions for the three structures are listed in Table 4.1. Subsequent analysis with PISA [250] showed that two of these subunits (chains B and C) form a homodimer with a buried interface of 1424 Å^2.

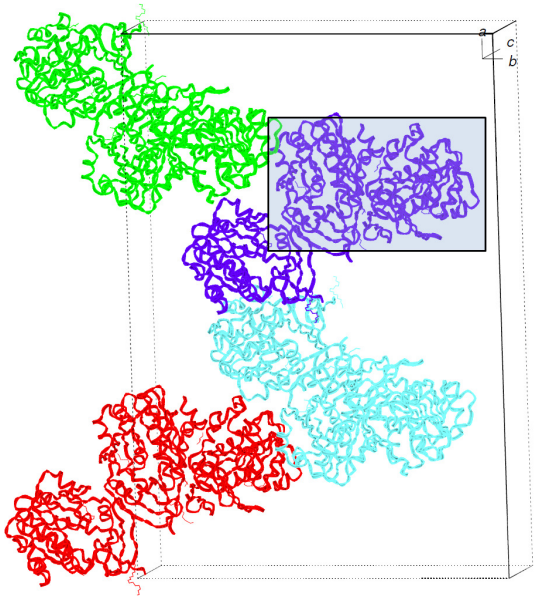

Figure 4.15: Diagram to illustrate the crystal packing of *Pf*SpdS-NACD crystallised in spacegroup C121. The diagram was obtained with the RCSB Atlas programme. Each colour represents the three monomers within the ASU of which two interact to form the homodimer (an example of such a homodimer is shown within the blue box).

*Pf*SpdS consists of two domains including an N-terminal β-sheet consisting of six anti-parallel strands and a catalytic domain consisting of a 7-stranded β-sheet flanked by 9 α-helices forming a Rossmann-like fold, which is typical of methyltransferases and nucleotide-binding proteins (Figure 4.16A) [97]. Each monomer contains its own independent active site, which is located between the two domains and is enclosed by a flexible gate-keeping loop (Figure 4.16A).

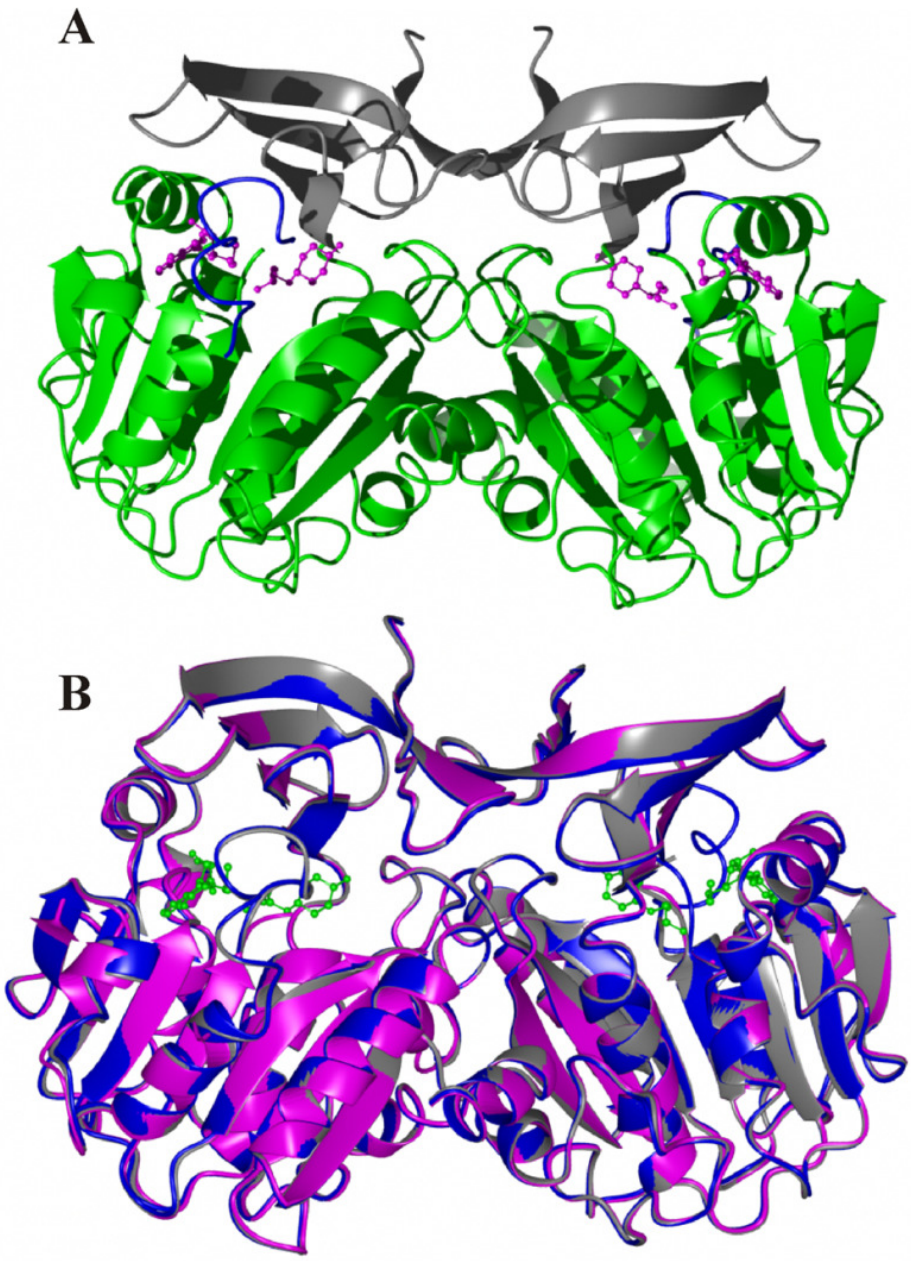

Figure 4.16: Overall fold of *Pf*SpdS (A) and superimposition of the solved crystal structures (B).
(A) The N-terminal and catalytic domains of each monomer are shown in grey and green, respectively. The active sites containing MTA and NACD are shown in magenta while the gate-keeping loops are in blue. (B) Alignment of the *Pf*SpdS-NACD (magenta), NACD-MTA (blue) and NAC-MTA (grey) crystal structures are shown. The active site ligands are shown in green.

The overall structures of all complexes obtained were nearly identical except for the gate-keeping loop, which was disordered in the *Pf*SpdS-NACD structure (residues 199-210 located between strand β-10 and helix α5) (Figure 4.16B). The RMSD value between *Pf*SpdS-NACD and the apo structure (2PSS), which was used for its molecular replacement during structure solving, is 0.21 Å. The RMSD values between the *Pf*SpdS-MTA structure (2HTE) and *Pf*SpdS-NAC-MTA and NACD-MTA structures are 0.18 Å and 0.29 Å, respectively. The active site consists of the two substrate-binding pockets for putrescine (identified here with NACD/NAC binding) and dcAdoMet (identified here with MTA binding) (Figure 4.16B). As will be

described in the next sections, the residues involved in substrate binding are conserved and were also shown to play a role in inhibitor binding.

4.3.5.3. Binding of NACD and MTA

In vitro studies on malaria parasites showed that the NACD inhibitor is effective in the micromolar range, with slightly improved activity compared to NAC, possibly due to the inclusion of an extra amine group on the cyclohexyl ring, which is predicted to align with the amine of 4MCHA (2PT9) and in turn aligns with the non-attacking nitrogen of putrescine. Subsequent crystallisation of *Pf*SpdS co-incubated with NACD and MTA confirmed the binding orientation of NACD within the putrescine-binding pocket (Figure 4.17). The N^3 amine on the cyclohexylamine ring is hydrogen bonded to Glu46 via a solvent molecule (2.8 Å) and directly to the side chain of Asp199 (3 Å). Even though density was observed for the solvent molecule that was identified in the dcAdoMet-4MCHA structure (2PT9) as being involved in hydrogen bonding with the amine of 4MCHA [119], a bond was not observed between Glu231 and one of the solvent molecules due to a distance of >6 Å between them. Tyr102 (3.4 Å) and the carbonyl group of Ser197 (3.2 Å) interact with the bridging amino group (N^2, the nitrogen connecting the aminopropyl chain of NACD to the cyclohexylamine ring) while Asp127 and Asp196 bind to the terminal amine N^1, which crosses the catalytic centre. These interactions confirm the *in silico* predictions of NACD binding (Figure 4.4). The gate-keeping loop was also clearly defined (Figure 4.17), which corroborates previous studies in which binding of a ligand to only the putrescine-binding pocket resulted in a flexible loop [119].

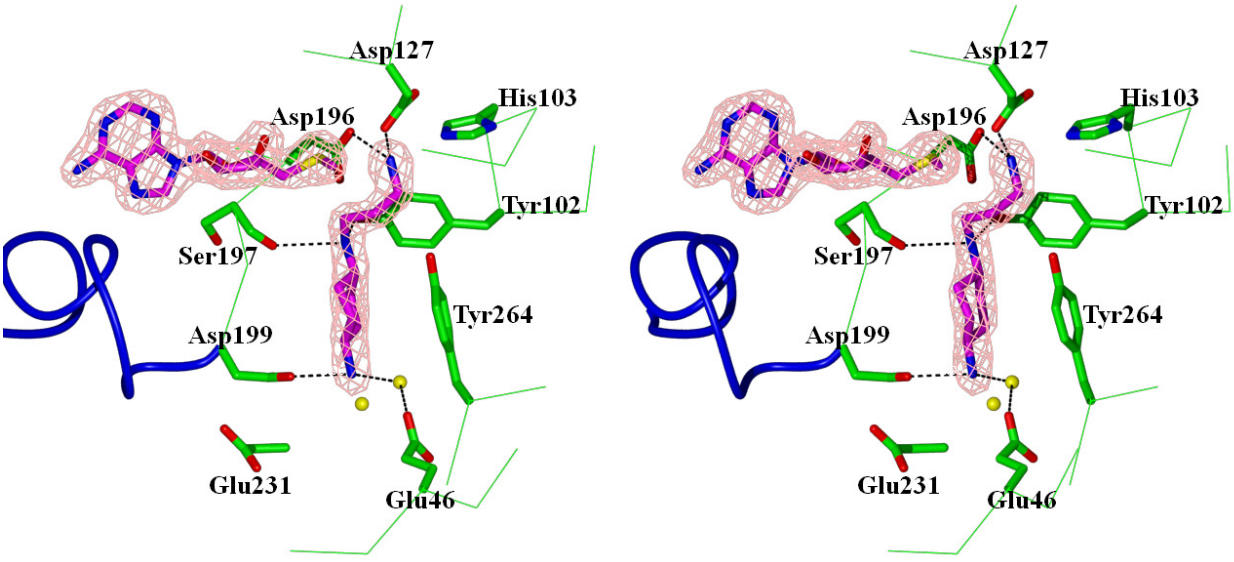

Figure 4.17: Stereo view of the *Pf*SpdS-NACD-MTA active site.
The MTA and NACD ligands together with their electron densities are shown in magenta. The residues involved in NACD binding are annotated while the gate-keeping loop is shown in blue. Solvent molecules involved in inhibitor binding are shown as yellow spheres.

The *Pf*SpdS-NACD-MTA structure superimposes well with the apo structure (2PSS) with an RMSD value of 0.31 Å, however, several conformational changes take place in order to accommodate the cyclohexylamine ring of NACD (Figure 4.18A). Most notably is the 90° rotation of Tyr264 to allow stacking of the aromatic side chain to the cyclohexylamine ring. The C_δ atom of Gln93 is shifted 1.7 Å to accommodate interactions with the C2 and C9 atoms of NACD. Ser197 also undergoes an almost 180° flip such that its carbonyl group can interact with the bridging amino group (Figures 4.17 and 4.18A). As previously predicted, Gln229 undergoes a significant conformational change in the presence of the inhibitor, which corroborates the DPM in which PhFs that represent binding of the attacking nitrogen of putrescine were identified by inclusion of the 2PT9 structure during negative image construction. Without the inclusion of this structure, NACD would probably not have been identified as a possible inhibitor due to the short distance of <1.86 Å between the position of Gln229 in the apo-state and the ring. The structures of *Pf*SpdS-NACD-MTA and dcAdoMet-4MCHA (2PT9) are very similar with an RMSD value of 0.33 Å. Residues involved in ligand binding are also conserved (Figure 4.18B).

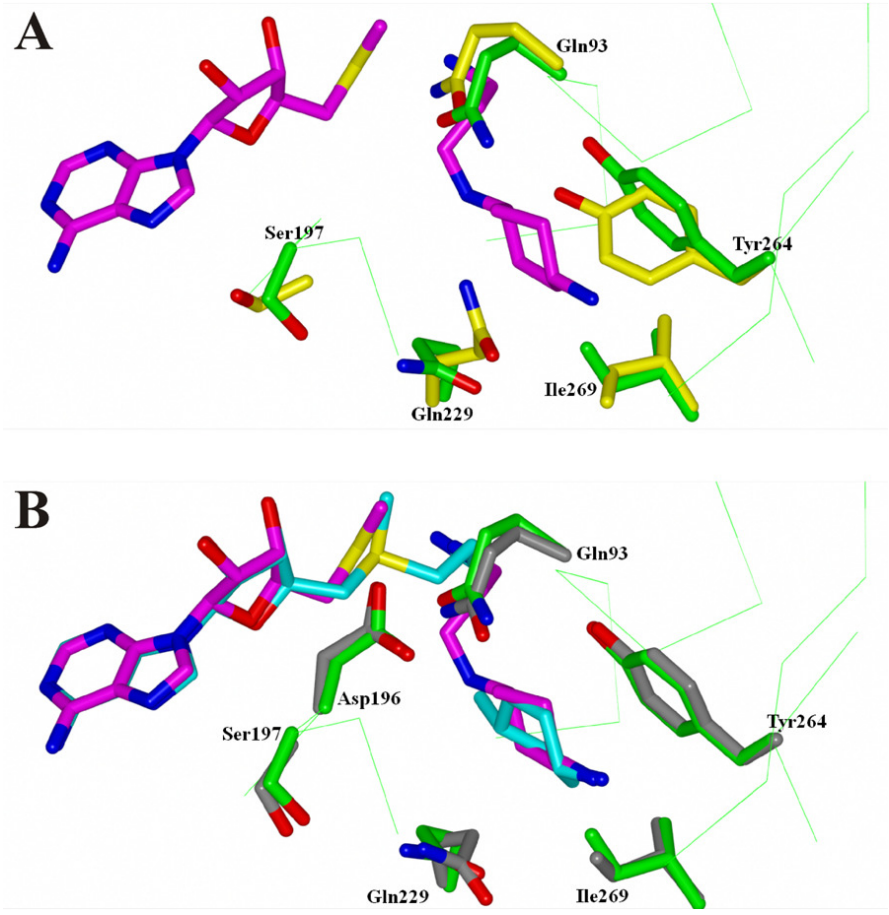

Figure 4.18: The active site of *Pf*SpdS-NACD-MTA superimposed with the 2PSS (A) and 2PT9 (B) crystal structures.
The MTA and NACD ligands of *Pf*SpdS-NACD-MTA are shown in magenta while the residues involved in NACD binding are shown in green. The corresponding residues of the apo structure are shown in yellow while those of the dcAdoMet-4MCHA (cyan) structure are shown in grey.

Protein crystallography provided important insights into the inhibitor efficiency of NACD in the presence of MTA, which binds within the DPM2 site and competes with both putrescine and dcAdoMet binding (section 4.3.1 and Figure 4.18). In addition and compared to 4MCHA, NACD forms additional binding interactions within the active site since the aminopropyl chain of NACD aligns with the terminal amine of dcAdoMet and further stabilises ligand binding (Figure 4.19). The structure also shows the binding of NACD to Asp199, which forms part of the gate-keeping loop.

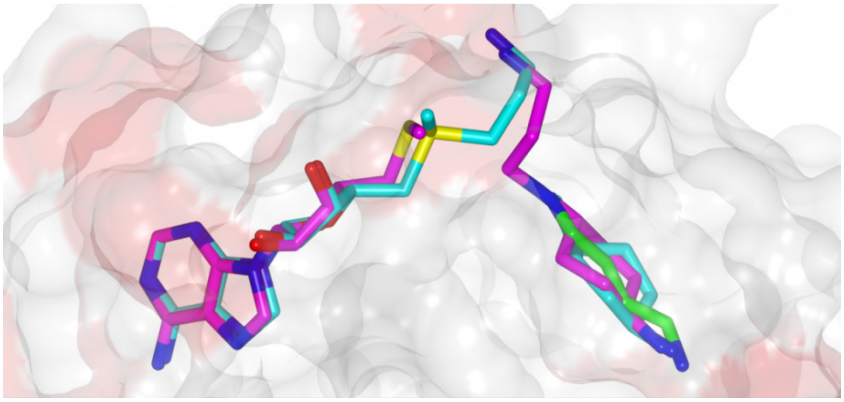

Figure 4.19: Electrostatic surface potential of the *Pf*SpdS active site.
Alignment of NACD and MTA (magenta), 4MCHA and dcAdoMet (2PT9, cyan) and putrescine (human structure 2O06, green). Blue represents nitrogen atoms, red represents oxygen and yellow represents sulphur atoms.

4.3.5.4. Binding of NACD

Crystallisation of *Pf*SpdS in the presence of only NACD did not show electron density of the inhibitor at the expected putrescine-binding site where NACD was located in the *Pf*SpdS-NACD-MTA structure. Instead the density map showed that NACD was bound within the dcAdoMet-binding pocket (Figure 4.20). The density was, however, much less defined than that observed for the NACD-MTA structure, which could be due to the flexibility of the aminopropyl chain and/or cyclohexylamine ring at this position. Furthermore, and as predicted from previous studies [119], the gate-keeping loop of the structure was disordered (residues 199 to 210) and loop flexibility could further have contributed to the flexibility of NACD. The suggestion that the sulphide atom of dcAdoMet or MTA is required for loop stabilisation is therefore supported by this result [97,119]. Binding of the inhibitor at the dcAdoMet-binding site could be substantiated by the ionic interactions that are detected between the carbonyl group of Cys146 and the terminal N^1 amino group (2.96 Å), Gln93 and the N^3 amine as well as between Ser197 and the bridging N^2 nitrogen (3.1 Å) of NACD. Residues that normally bind the natural substrate such as Glu147, Gln72 and Asp178 can also stabilise the interaction and favour the binding of NACD at this position (Figure 4.20).

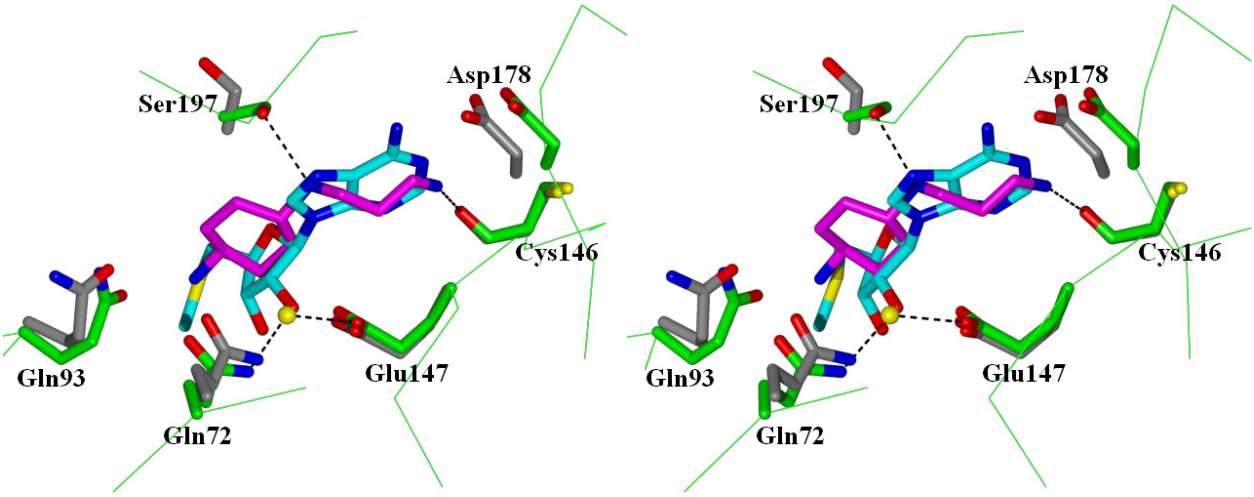

Figure 4.20: Stereo view of the *Pf*SpdS-NACD active site.
The MTA (2HTE) and NACD ligands are shown in cyan and magenta, respectively. Residues involved in NACD binding are annotated and shown in green while the corresponding residues of 2HTE are shown in grey. The solvent molecule is shown as a yellow sphere.

The cyclohexylamine ring is positioned perpendicular to the ribosyl group of MTA and the N^1 and N^2 amino groups of the inhibitor overlap with N^1 and N^9 from MTA, which allows NACD to form interactions with Cys146 and Ser197, respectively (Figure 4.20). Interestingly, a water molecule was identified in the *Pf*SpdS-NACD structure that occupies the site of one of the hydroxyls on the ribosyl moiety of MTA. Previously, it was shown that solvent molecules do not mediate interactions between ligands within the dcAdoMet-binding site and the active site residues [119]. However, in the absence of the ribosyl moiety, a solvent molecule was detected that forms hydrogen bonds with Gln72 (2.6 Å) and Glu147 (2.7 Å) and may thereby stabilise the ring moiety of NACD (3.1-3.3 Å) (Figure 4.20).

Superimposition of the *Pf*SpdS-NACD structure with the MTA complex (2HTE) showed several changes in active site residues to accommodate inhibitor binding. Ser197 rotated 90° towards NACD to form an interaction with the bridging amino group. Gln93 shifted 2.2 Å towards the amine group on the cyclohexylamine ring (Figure 4.20). The cause of the movement of Asp178 away from the ligand to a distance of >7 Å is unclear.

These results showed that the efficiency of the NACD compound may be more pronounced in the presence of MTA, which shifts binding to the putrescine-binding pocket. In the presence of MTA the gate-keeping loop also becomes inflexible and may be locked in a fixed or closed position, resulting in an increase in the inhibitor binding efficiency. Nonetheless, the crystal

structures of *Pf*SpdS in complex with NACD validated the *in vitro* inhibition results as well as the use of a DPM to identify novel lead compounds.

4.3.5.5. Binding of NAC

The last structure that was solved was of *Pf*SpdS co-crystallised with NAC and MTA. Similar results to that of the NACD-MTA complex were expected, except for the absence of the terminal amine on the cyclohexyl ring. Docking results of NAC predicted a very similar binding pose to that of NACD (Figure 4.4). However, upon solving of the crystal structure at a lower resolution than that of the NACD structures (2.39 Å versus 1.9 Å), some unexpected results were observed. Firstly, density of NAC within the putrescine-binding pocket that could fit the ligand could not be identified but instead showed the presence of two well defined solvent molecules occupying the sites where the N^1 and N^3 nitrogen atoms of the ligand were expected to be located (Figure 4.21). Furthermore, even though NAC was absent, the residues previously identified as being involved in NACD binding were orientated in such a way that indicated the presence of the ligand. As expected, binding of MTA resulted in the gate-keeping loop being inflexible and could therefore be solved in the structure (Figure 4.21).

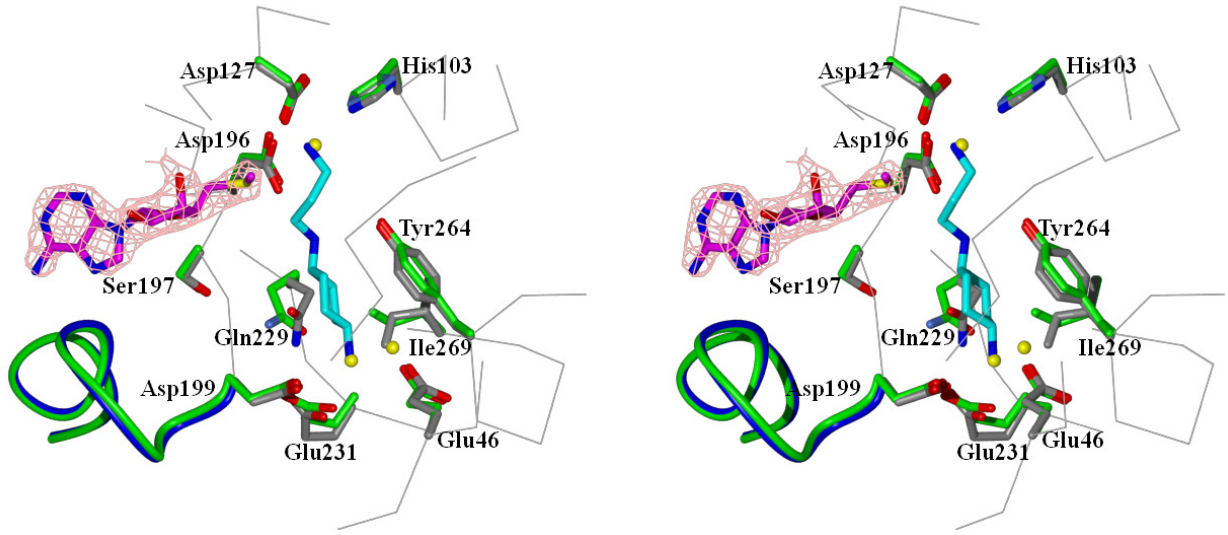

Figure 4.21: Stereo view of the *Pf*SpdS-NAC-MTA active site.
NACD from the *Pf*SpdS-NACD-MTA structure is shown in cyan while MTA from the NAC-MTA structure is shown in magenta together with its electron density. Residues previously shown to be involved in NACD binding are annotated and shown in green while the corresponding residues of the NAC-MTA structure are in grey. The gate-keeping loops are also shown. The solvent molecules are shown as yellow spheres.

The orientations of the residues, which suggested a ligand-bound state of the protein becomes even more obvious when the *Pf*SpdS-NAC-MTA structure is superimposed with the apo structure (2PSS) (Figure 4.22). Tyr264 is positioned in such a way to allow stacking against a ligand with its aromatic side chain, Ser197 is orientated perpendicular to that of the residue in the

apo structure while Gln229 and Glu231 are also shifted as if to participate in interactions with the ligand. Furthermore, even though the majority of the solvent molecules in the active site of the NAC-MTA structure align with that of the apo one, the molecule occupying the site where the non-attacking nitrogen (N^1) of NAC is predicted to be positioned is not conserved (Figures 4.21 and 4.22) and could indicate that this molecule fulfills the binding interactions with the repositioned residues in the absence of NAC.

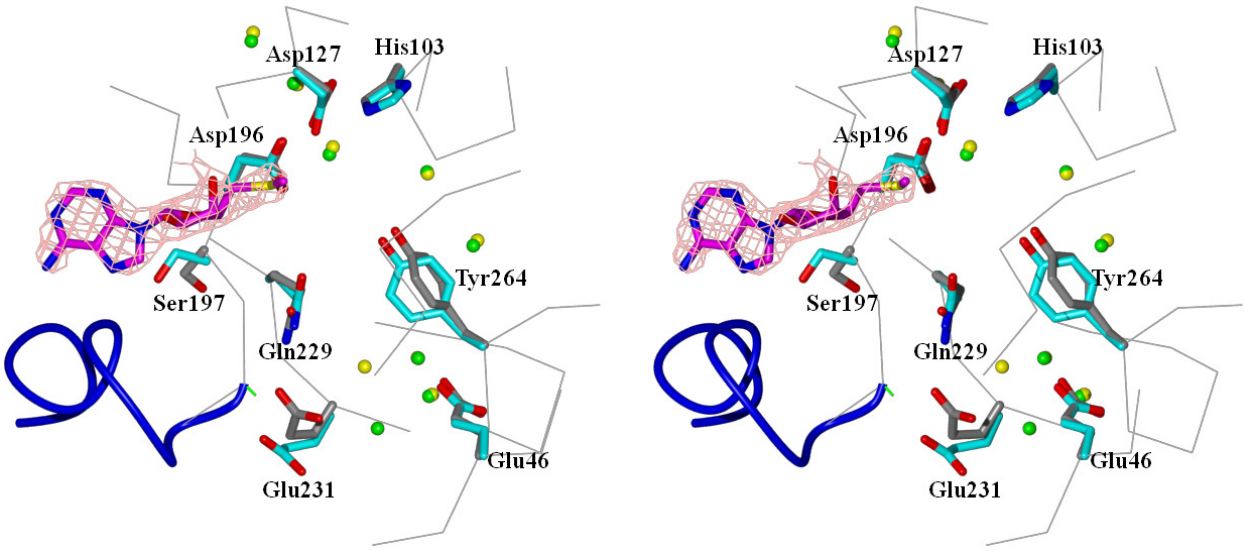

Figure 4.22: Stereo view of the *Pf*SpdS-NAC-MTA active site superimposed with the apo structure. MTA from the NAC-MTA structure is shown in magenta together with its electron density. Residues previously shown to be involved in NACD binding are annotated and shown in grey for the NAC-MTA structure while the corresponding residues of the apo structure are in cyan. The gate-keeping loop of *Pf*SpdS-NAC-MTA is also shown as a blue ribbon. The solvent molecules belonging to the NAC-MTA structure are shown as yellow spheres while that of the apo structure are in green.

These results show that either the flexibility of the ligand was too high such that density could not be detected where NAC was predicted to bind, or the protein was not co-crystallised with the inhibitor. Another possibility could be that the observed residue orientations that were previously shown with the NACD-MTA structure to accommodate ligand binding could indicate that the ligand was in fact present within the active site but was replaced with solvent molecules during crystal soaking in the cryo protectant due to the weaker binding interaction of the ligand within the active site compared to NACD. No direct conclusions could therefore be obtained from the crystal structure of *Pf*SpdS bound with NAC. However, based on the inhibitory efficiency of NAC as well as the detailed results obtained from the NACD-MTA crystal structure it is likely that the binding pose predicted in Figure 4.4 pertains to that of NAC binding within *Pf*SpdS.

4.4. Discussion

The identification of effective inhibitors against SpdS with the application of ligand- or receptor-based approaches has proven difficult and largely ineffective [226,251]. 4MCHA was identified with a ligand-based approach by synthesising putrescine analogues and, despite its poor target specificity [98], still represents the best inhibitor of *Pf*SpdS to date [220]. In 2008 the first structure-based study for *Pf*SpdS was released and although no promising leads were identified it provided a proof of principle for the application of *in silico* methods to screen thousands of compounds for subsequent *in vitro* testing [251]. Due to the lack of highly effective and specific inhibitors of *Pf*SpdS activity, we decided to follow a different approach for inhibitor design, which could add to the list of current *Pf*SpdS inhibitors (Table 4.2).

Table 4.2: Inhibitors tested *in vitro* on *Pf*SpdS or in whole-cell assays against *P. falciparum*.

Only inhibitors for which *in vitro Pf*SpdS inhibitory values are available are included, which are listed from the most to the least effective. When available, the IC_{50} values of the inhibitors against *in vitro P. falciparum* are also included.

Inhibitors	K_i (µM)	IC_{50} (µM)	Binding cavity	Size (Da)
4MCHA	1.4	34.2	putrescine and unknown	113
NAC	2.8	105	-	159
NACD	-	81	putrescine (in presence of MTA)	281
APE	6.5	83.3	putrescine	85
AdoDATO	8.5	-	dcAdoMet and putrescine	425
Cyclohexylamine	19.7	198	putrescine	99
2-Mercaptoethylamine	76	254	unknown	77
APA	84	1.0	putrescine	90
MTA	159	-	dcAdoMet	313
Dicyclohexylamine	>1000	342	unknown	181

Interaction of the inhibitors within the putrescine, dcAdoMet, the entire active site or unknown binding sites is indicated. All the results were obtained from [98] except for the AdoDATO data [119].

The DPM computational approach used in this study allowed individual pharmacophore sites to be probed using distinct chemical moieties that displayed favourable binding properties. Pharmacophore modelling therefore provided a powerful tool for extracting representative biologically active components from both inhibitor ligands and their intended protein target receptors. It also allowed for the incorporation of information from previous studies as well as information derived during the discovery process. The methodology furthermore addressed the problem of protein flexibility during structure-based drug design, which is one of the major challenges that computational chemists currently face [229,230]. This approach resulted in the identification of novel inhibitors against SpdS of *P. falciparum*, which were tested on the recombinant *Pf*SpdS protein (Table 4.2).

Binding cavities were selected to identify specific binding hotspots that could be used in the identification of ligands. For this purpose the *Pf*SpdS active site was divided into four binding cavities. Most relevant to this study was the DPM2 binding cavity, which was selected to identify compounds that favourably bind within the putrescine- and a part of the dcAdoMet-binding sites and therefore represented an area that has not been studied. The premise for selecting this binding cavity is based on the knowledge that SpdS catalyses the aminoproyl transfer from dcAdoMet to putrescine, wherein product release is mediated by a gate-keeping loop that opens and closes over the active site. It was therefore hypothesised that compounds binding favourably to the DPM2 cavity will also form interactions with residues from the loop (Ser197 and Asp199) and thereby maintain the loop in a closed conformation for longer periods of time resulting in increased inhibitor potency. Alternatively, the loop may be locked in a closed position, which inactivates the protein indefinitely.

Currently, AdoDATO is the only known inhibitor that crosses the negatively-charged catalytic centre of *Pf*SpdS. The crossing of the catalytic centre by the aliphatic aminopentyl chain of AdoDATO can be attributed to the substrate-like characteristics of this compound, which are strong enough to overcome this unfavourable interaction. The 4MCHA and APE inhibitors are more effective against *Pf*SpdS than AdoDATO [98], and they are also much smaller molecules with sizes of 85 and 113 Da compared to the 425 Da of AdoDATO (Table 4.2). Furthermore, it is known that the strong inhibition characteristics of 4MCHA and APE are due to cooperative binding with either dcAdoMet or MTA. It can therefore be postulated that the higher K_i value of AdoDATO is partly due to the unfavourable interactions of the aliphatic part of the aminopropyl moiety, which crosses the negatively-charged catalytic centre. This highlights the importance of finding chemical entities that are able to link ligands bound within the dcAdoMet-binding cavity to ones within the putrescine-binding site by bridging the catalytic centre. It is also known that the catalytic centre binds positive ionisable groups to catalyse the transfer of an aminopropyl group and the residues involved in binding the attacking nitrogen of putrescine are Tyr102, Asp196 and the backbone carbonyl group of Ser197 [97]. Therefore in this study, the PhFs and binding poses of AdoDATO, dcAdoMet and 4MCHA were used to derive compounds, which could bridge the catalytic centre and favourably bind within this region.

The compound NACD was identified by taking into account these considerations and represents a basic scaffold for an inhibitor of *Pf*SpdS. NACD docking to *Pf*SpdS was used to predict its binding poses and it was shown that the cyclohexylamine moiety binds in a similar manner to

4MCHA. It was anticipated that hydrogen bond formations would reduce the penalty that an aliphatic carbon would have by binding within the catalytic centre and thereby increase the binding affinity as well as inhibitory activity. The aminopropyl chain of NACD was also predicted to bind in the same cavity as the aminopropyl chain of dcAdoMet. Due to the unavailability of NACD at the time, NAC was identified as a similar, commercially available compound. The compound is an analogue of cyclohexylamine containing an additional aminopropyl chain. Similar binding poses and hydrogen bond patterns as NACD were therefore predicted, except for the missing amino group. This made NAC a good alternative to test and subsequent enzyme kinetics of this compound showed a high inhibitor activity against *Pf*SpdS with a K_i of 2.8 µM, which is comparable to that of 4MCHA (Table 4.2). Kinetics also showed competitive binding, which suggested that the interaction involves competitive interaction with both putrescine and dcAdoMet. The low K_i could be due to specific hydrogen bond formation of NAC with *Pf*SpdS, which can only be true if NAC binds in the predicted docking pose by bridging the catalytic centre and if the aminopropyl chain binds in the aminopropyl binding pocket of the dcAdoMet cavity. This binding mode of NAC would also accommodate the simultaneous binding of MTA, which would allow the gate-keeping loop to close over the active site. Furthermore, the ability of the compound to form hydrogen bonds with residues Tyr102 and Ser197 may significantly contribute to the strong binding of the compound in the active site, which could play a role in the stabilisation of the gate-keeping loop and to keep it closed for a longer period over the active site. A similar phenomenon was observed in the co-crystallisation of *Pf*SpdS and 4MCHA where the binding of 4MCHA could only be resolved in the presence of dcAdoMet. It was therefore suggested by the authors that dcAdoMet binding occurs prior to 4MCHA or putrescine binding hence resulting in inhibition or catalysis, respectively [119]. A similar phenomenon was observed for putrescine and MTA binding to human SpdS [97].With this information in mind, it can be speculated that, if the kinetic data holds true and NAC also requires cooperative binding of a second compound within the dcAdoMet cavity, then the true K_i of NAC is observed when MTA is bound within the dcAdoMet-binding pocket.

Even though NAC was shown to be extremely effective on the recombinant enzyme level, *in vitro* determination of the effect of NAC and NACD on the parasite cultures resulted in 50% growth inhibition in the micromolar range, which is approximately double the IC_{50} of 4MCHA and in the range of inhibition provided by APE (Table 4.2). These results suggest poor uptake or instability problems of the compounds *in vitro*. Analyses of the druggability of NAC showed that it conforms to the Lipinski's rule of five, which makes the drug orally active [252]. NAC

contains only two hydrogen bond donors, no hydrogen bond acceptors, it has a LogP value of 1.57 and the size of the compound is 159 Da, which is below the required limit of 500 Da. Alternative drug-delivery strategies may improve the *in vitro* whole-cell activity of these compounds to acceptable ranges (<1 µM) as specified by e.g. the MMV (http://www.mmv.org/). However, preliminary results provided by the co-inhibition of *Pf*SpdS with either NAC or NACD and the rate-limiting enzymes of the polyamine pathway showed additive inhibition. These results indicate that the specific and simultaneous inactivation of the parasite-specific bifunctional *Pf*AdoMetDC/ODC enzyme together with the flux-determining *Pf*SpdS enzyme could result in improved inhibitory effects and lead to possible cessation of *in vivo* synthesised polyamines. Currently, inhibitors such as MDL73811, DFMO and 4MCHA can be used to simultaneously target these enzymes but these only result in cytostatic growth effects and we therefore need to find strategies beyond those that are currently available. Future studies, in combination with the crystal structure results, could improve the inhibition efficiency, target specificity and drug delivery of these compounds that may have an increased inhibitory effect on the parasite cultures by targeting the polyamine biosynthetic pathway.

Protein crystallisation is an extremely valuable tool in the field of drug discovery for the validation of predicted binding sites of inhibitors as well as to obtain insights into the improvement of target specificity. In this study, the *in silico* predicted binding poses and active site interactions of NAC and NACD with *Pf*SpdS were therefore confirmed via the co-crystallisation of these compounds with the protein. Analyses of near-UV CD results as well as geometric analyses of the residues with Ramachandran plots provided an early indication of different binding interactions of NAC and NACD in the presence or absence of MTA. The CD results showed a difference in the tertiary structures depending on the presence of a substrate in the dcAdoMet-binding cavity. Furthermore, the presence of Glu231 in the outlier regions of the Ramachandran plots when both the binding cavities were filled indicated that this residue in the NACD crystal structure may not be involved in inhibitor binding. This could be hypothesised since it was previously shown that this residue orientates itself differently in the presence of both 4MCHA and dcAdoMet [119]. The residue is therefore strained in the presence of the ligand in such a way as to accommodate the ring moiety of the inhibitor.

The crystal structure of *Pf*SpdS-NACD-MTA confirmed the *in silico* predicted binding poses and highlighted the interactions of this inhibitor within the active site that allowed it to display its inhibitory properties. The observed interactions also showed how the flanking acidic regions

of the putrescine-binding pocket accommodates the ligand with its terminal positive ionisable groups, which forms hydrogen bonds with Glu231 and Glu46 at the non-attacking nitrogen, and Asp127 and Asp196 at the attacking nitrogen. Hydrogen bonds involving Ser197 and Tyr102 with the bridging nitrogen group also showed how the ligand is accommodated despite its presence within the hydrophobic cavity of the putrescine-binding site. Furthermore, the gate-keeping loop became inflexible and therefore enabled diffraction data collection of the residues. This indicates that MTA followed by inhibitor binding resulted in the closure of the loop, which could be mediated by the sulphide atom (as previously suggested [97,119]) and/or binding of the ligand, respectively. This hypothesis was confirmed with the crystal structure of *Pf*SpdS-NACD where the loop was not resolved either due to the absence of MTA or the binding of NACD within the dcAdoMet cavity and therefore the absence of stabilising interactions with the loop. However, a different hypothesis is proposed here where the sulphide atom of MTA is not primarily responsible for loop stabilisation but as a result of the contribution of various interactions of both the ligands with the loop in such a way that it becomes inflexible. From the 10 residues that constitute the loop spanning residues Asp196 to Glu205, six interactions are formed between the two ligands and residues Asp196, Ser197, Ser198, Asp199, Pro203 and Ala204. It therefore seems that the contribution of several stabilising interactions could close the loop over the active site. In fact, only a single interaction mediated by the sulphide atom could be deduced from the 2PT9 crystal structure and involves Asp127, which would hardly constitute loop stabilisation to a residue that is not even present on the loop.

Furthermore, even though electron density of NAC in the *Pf*SpdS-NAC-MTA was not detected, it could be deduced that the NAC was present within putrescine-binding site since MTA was bound in the dcAdoMet cavity and the conformational changes of the residues that were identified in the NACD-MTA structure were similar. The loop was also stabilised in this structure, which indicates that both binding sites were filled. Therefore the improved inhibitory activity of NACD is predicted to be due to the additional amino group on the ring moiety, which forms ionic interactions within the acidic region of the non-attacking nitrogen of the active site. This additional nitrogen also improved stability of ligand binding such that the ligand did not diffuse out during cryo protectant soaking as is suggested to be the case for NAC.

The *Pf*SpdS-NACD-MTA structure showed that the sulphide atom of MTA may additionally interact with the aminopropyl chain of NACD and thereby contribute to its binding within the active site. It can therefore be deduced that a compound that includes the chemical properties of

NACD as well as the essential elements of MTA may represent an important candidate to test, which would still follow the strategy of bridging the catalytic centre of *Pf*SpdS. Previous suggestions by P. B. Burger include N^3-cyclohexylpentane-1,3,5-triaminium (NACDS), N^2-cyclohexylbutane-1,2,4-triaminium (NACDS-alternative) and N^3-[(1*R*,4*R*)-4-ammonio-cyclohexyl]pentane-1,3,5-triaminium (NACDSW) as derivatives of NAC and NACD, whereby the extra groups (boxed in Figure 4.23) can bind within the sulphide-binding cavity of MTA and thereby display the combined inhibitory effects of NACD and MTA.

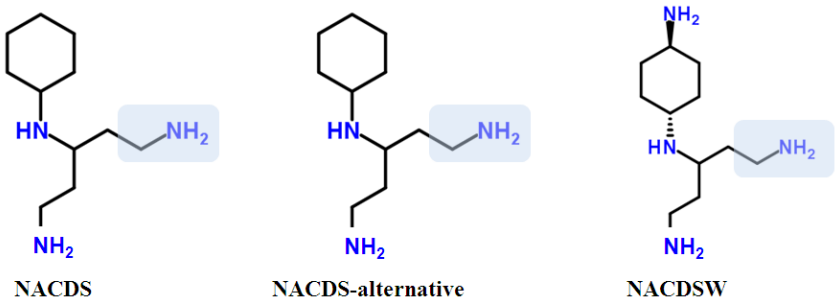

Figure 4.23: Derivatives of NAC and NACD as alternative chemical compounds to test for inhibition of *Pf*SpdS activity.
Chemical structures were obtained from ChemSpider (http://www.chemspider.com/) where nitrogen and amine groups are shown in blue. The boxed areas represent the chemical entities that are predicted to bind in the sulphide-binding cavity of MTA. Abbreviations: NACDS, N^3-cyclohexylpentane-1,3,5-triaminium; NACDS-alternative, N^2-cyclohexylbutane-1,2,4-triaminium; NACDSW, N^3-[(1*R*,4*R*)-4-ammonio-cyclohexyl]pentane-1,3,5-triaminium.

The opening of the gate-keeping loop once the aminopropyl chain of dcAdoMet has been transferred to putrescine resulting in the formation of MTA and spermidine also indicates that the loop opening following catalysis may be mediated by the interactions of the aminopropyl chain. One would expect that the presence of MTA would relieve the loop closure such that the reaction products can be released while dcAdoMet would stabilise loop closure. A crystal structure containing putrescine would provide more information on the possible role of the aminopropyl chain in loop movement. An important aspect to take into account in terms of identifying a drug that locks the *Pf*SpdS gate-keeping loop in closed formation is the half-life of *Pf*SpdS. The stability of *Pf*SpdS enzyme has not been determined but it is generally known that SpdS is more stable than AdoMetDC and ODC [253] and studies on mouse mammary epithelium showed a half-life of >12 h [254]. In *P. falciparum* it has been shown that transcription occurs with a just-in-time manufacturing process whereby induction of a gene occurs once per intra-erythrocytic cycle and only at a time when it is required [4]. The drug candidate therefore needs to be specific enough such that its inhibitory properties will have an effect during this period. In addition, target specificity therefore becomes a critical issue such that inhibitor binding does not result in prolonged inhibition of the host protein if the drug is not

target specific. Future studies include testing of the compounds identified with the DPM against mammalian cell lines since the active site of SpdS is highly conserved. As can be seen in Figure 4.24 superimposition of the *Pf*SpdS-NACD-MTA structure with the human protein (2O06, [97]) shows that only His103 (corresponding to hGln80) is not conserved between the two proteins. Whether this change is significant enough to produce a target specific response should be determined *in vitro*.

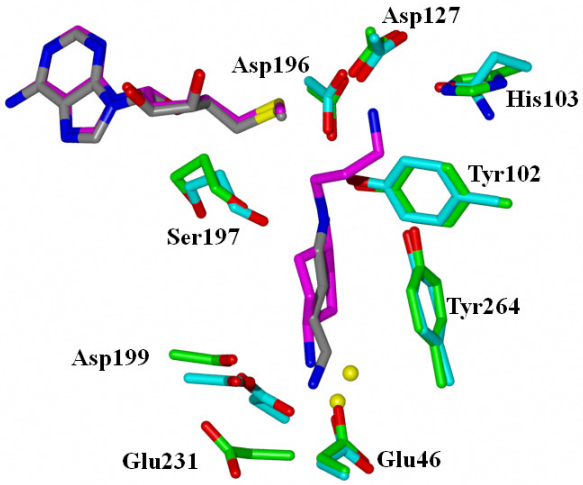

Figure 4.24: The *Pf*SpdS-NACD-MTA active site superimposed with the human structure.
MTA and NACD from the *Pf*SpdS-NACD-MTA structure are shown in magenta while MTA and putrescine from the human structure (2O06) is shown in grey [97]. Residues previously shown to be involved in NACD binding are annotated and shown in green while the corresponding residues of the human structure are in cyan. The solvent molecules belonging to the NACD-MTA structure are shown as yellow spheres. His103 is the only unique *P. falciparum* residue within the active site that is involved in NACD binding.

4.5. Conclusion

The compounds identified in this study have been shown to cross the catalytic centre of *Pf*SpdS in an energetically favourable manner by hydrogen bonding to Tyr102 and Ser197, and cooperatively bind MTA within the dcAdoMet cavity. Inhibition was also in the range of 4MCHA activity, while improved potency was expected since the inhibitor competes with both putrescine and dcAdoMet. Protein X-ray crystallography subsequently confirmed the binding of the novel inhibitory compound within the *Pf*SpdS active site and showed how NACD is stabilised within the active site by additional hydrogen bonds. Novel insights into the stabilisation of the gate-keeping loop of the holo-protein were also obtained from the structures.

Therefore the promising results of these two inhibitors which target both the putrescine and dcAdoMet binding activities emphasise the value of incorporating a “dynamic”, receptor-based pharmacophore model and represent a valuable tool for the future design of possible therapeutics.